Profiling of histone H1 variants and changes on genome architecture and gene expression upon histone H1 depletion in breast cancer cells

Núria Serna-Pujol[1,#], Mónica Salinas-Pena[1,#], Francesca Mugianesi[2,#], François Le Dily[3], Marc A. Marti-Renom[2,3,4,5], Albert Jordan[1,*]

[1] Molecular Biology Institute of Barcelona (IBMB-CSIC), Barcelona, 08028, Spain
[2] CNAG-CRG, Centre for Genomic Regulation, The Barcelona Institute of Science and Technology, Baldiri Reixac 4, Barcelona, 08028, Spain
[3] Centre for Genomic Regulation, The Barcelona Institute for Science and Technology, Carrer del Doctor Aiguader 88, Barcelona, 08003, Spain
[4] Pompeu Fabra University, Doctor Aiguader 88, Barcelona, 08003, Spain
[5] ICREA, Pg. Lluís Companys 23, 08010 Barcelona, Spain

[#] These authors contributed equally to this work.

*To whom correspondence should be addressed. Tel: +34 93 402 0487; Fax: +34 93 403 4979; Email: Albert.jordan@ibmb.csic.es

Running title: **Consequences of H1 depletion on genome architecture**

Abstract

Human somatic cells may contain up to seven members of the histone H1 family contributing to chromatin compaction and its regulation. In breast cancer cells, knock-down (KD) of each H1 variant results in specific gene expression changes. We have previously shown that combined KD of H1.2 and H1.4 (H1 KD) deregulates many genes, promotes the appearance of accessibility sites genome wide and triggers an interferon response via activation of heterochromatic repeats. Here we describe for the first time ChIP-seq profiling of five endogenous H1 variants at the same time, obtaining that H1 variants are differentially distributed at low (H1.2, H1.5, H1.0) and high (H1X, H1.4) GC content regions**.** Further, we report that H1 KD promotes redistribution of some of the variants and changes on genome architecture. H1 KD decreased topologically associating domain (TAD) border strength as well as its interactions, both inter- and intra-TAD. In addition, many TADs presented a coordinated gene expression response to H1 KD. Up-regulated genes accumulate within TADs with low gene density and high H1.2 content. In conclusion, our data suggests that the equilibrium between distinct histone H1 variants helps maintaining the topological organization of the genome and the proper expression of particular gene programs.

INTRODUCTION

DNA is packaged within the nucleus to efficiently regulate nuclear processes. Chromatin packing involves several hierarchical levels of organization that have been recently discovered by chromosome conformation capture techniques, among others. First, at megabases scale, the genome can be segregated into the so-called A and B self-associating compartments. A compartment represents active, accessible chromatin occupying a more central position in the nucleus. B compartment corresponds to heterochromatin and gene deserts enriched at the nuclear periphery (1). Second, topological associating domains (TADs), which are submegabase structures, interact more frequently within themselves than with the rest of the genome (2–4). TADs are conserved across species and cell types and show a coordinated transcriptional status (5, 6). Third, these domains are formed by assemblies of chromatin loops that, ultimately, are composed by nucleosomes. Each nucleosome consists of an octamer of core histones (H2A, H2B, H3 and H4) around which ~147 base pairs (bp) of DNA are wrapped. Histone H1 binds to the nucleosome with ~10 bp of DNA at both the entry and the exit sites of the nucleosome core particle (7). Although participation in higher-order-chromatin structures is the function classically attributed to histone H1, its functional association with genome compartments and TADs has been barely studied. Furthermore, histone H1 cannot be seen any longer as a general condenser, as it plays a dynamic role in chromatin regulation (8, 9).

Histone H1 family is evolutionary diverse and human somatic cells may contain up to seven H1 variants (H1.1 to H1.5, H1.0 and H1X). H1.1-H1.5 variants are expressed in a replication-dependent manner while H1.0 and H1X are replication-independent. H1.2 to H1.5 and H1X are ubiquitously expressed, H1.1 is restricted to certain tissues and H1.0 accumulates in terminally differentiated cells (8, 10, 11).

Several studies support the idea that H1 variants are not fully redundant, but variant-specificity exists. In breast cancer cells, knock-down (KD) of each individual H1 variant deregulates a different subset of genes (12, 13). Another evidence of functional specificity among H1 variants is their interaction with different protein partners as well as their non-random distribution genome-wide (13–19). Thus, H1 variants show variant-specific genomic distribution within the nucleus, in a cell-type specific manner. However, experimental designs have been biased by the lack of specific H1 variants ChIP-grade antibodies, so different alternatives were used to map exogenous H1 proteins. In mouse embryonic stem cells (ESCs), by using a knock-in system of tagged H1 variants coupled with ChIP-seq, H1c and H1d (H1.2 and H1.3 orthologs) were found to be depleted from high GC, gene-rich regions and abundant at major satellites (16). In IMR90 cells and through DamID technology, H1.2-H1.5 showed similar profiles and were depleted from CpG-dense and regulatory regions while H1.1 displayed a different pattern (17). In T47D breast cancer cells ChIP-seq of endogenous H1.2 and H1X was performed. For the other variants, histones tagged with the hemaglutinin (HA) peptide were stably expressed and ChIP-seq was performed using an anti-HA antibody (18). Results showed that all H1 variants are depleted at promoters of active genes, but data also uncovered variant-specific features. Tagged-H1s exhibited similar distribution patterns, being enriched at high GC regions. Endogenous H1.2 and H1X showed opposite profiles: while H1.2 was found in low GC regions and lamina-associated domains (LADs), H1X strongly correlated with GC content and was associated to RNA polymerase II (RNApol II) binding sites (13, 18). Profiling of single endogenous H1.5 and H1.0 have been also achieved in human cells. In IMR90, H1.5 binding correlated with depletion of RNApol II and repression of target genes in differentiated cells (15). In skin fibroblasts, mapping of H1.0 revealed its correlation with GC content and abundancy at gene-rich chromosomes (19).

All these results lead to a complex scenario when comparing H1 variants distribution from different studies or cell lines. For that, genome compartmentalization methods could ease comprehension of the data. Our recent studies support that Giemsa bands (G bands) are useful as epigenetic units to investigate the differential distribution of linker histones (20). When evaluating H1 variants abundance at G bands, several epigenetic features are also recapitulated and their correlation with GC content, transcription factors binding, chromatin accessibility or topology, among others, can be inferred. Thus, T47D H1.2 and H1X showed an opposite distribution among G bands, being H1.2 associated to low GC bands and H1X to high GC bands. A strong correlation between B compartment, TADs presenting a high H1.2/H1X ratio, low GC bands and compact, late-replicating chromatin was found. These results suggest that H1 variants may play an active role in chromatin 3D organization.

Although no functional Hi-C experiments have been performed in H1-depleted human cells, the direct involvement of linker histones in chromatin structure has been proved in mouse ESCs. Hi-C experiments were performed in wild-type and H1-triple knockout (TKO) ESCs. In H1 TKO, TADs structures remained largely unaltered but other structural changes were observed. Increased inter-TAD interactions correlated with changes in active histone marks, an increase in the number of DNA hypersensitivity sites and decreased DNA methylation (21). These results point to an essential role of histone H1 in modulating local chromatin organization.

To study consequences of significant H1 depletion in human cells, we previously generated a derivative T47D cell line containing a short-hairpin-RNA that affects expression of several H1 genes (H1 KD), but mainly H1.2 and H1.4 at the protein level (22). H1 total levels were reduced to ≈70% and more severe consequences were observed, compared to those occurred in single-H1 KDs (12, 13). Upon combined H1 depletion, heterochromatic repeats (including satellites and endogenous retroviruses) were highly expressed, triggering a strong interferon response.

Here, we aim to further understand how H1 variants are specifically distributed throughout the genome as well as the consequences of H1 depletion in chromatin

organization and nuclear homeostasis. We have performed ChIP-seq in T47D breast cancer cells, and Hi-C experiments under basal conditions and after combined depletion of H1.2 and H1.4 (H1 KD). Profiling of endogenous H1 variants revealed that two profiles of H1 co-exist in the cell. H1.2, H1.5 and H1.0 are abundant at low GC regions while H1.4 and H1X preferentially co-localize at high GC domains. Profiling of H1s within chromatin states ('colors') showed that all H1 variants are enriched at heterochromatin and low-activity chromatin, but H1X was more abundant than the others at promoters. H1.4 profile overlapped H3K9me3 distribution. After multiple H1 depletion, slight H1 redistribution occurred; H1.4 profile was slightly switched towards the H1.2 group and H1X was decreased at heterochromatin and increased in almost all other chromatin states. Using Hi-C to measure changes in genome architecture upon H1 KD, shifts between A and B compartments were observed as well as within compartments, similarly in both directions. Although TADs hardly changed its size or distribution upon H1 KD, TAD border strength and intra- or inter-TAD interactions were reduced. Chromatin accessibility increased genome-wide, especially at A compartment, where H3K9me3 abundance was reduced. B compartment, where H1.2 was enriched at basal conditions, also showed a more open state and loss of broad H3K9me3 peaks, pointing to heterochromatin disorganization. Regarding gene expression deregulation upon H1 KD, a coordinated gene response occurred within TADs. Besides, up-regulated genes accumulated in TADs with low basal gene expression and high H1.2 content. Three-dimensional (3D) modeling of TADs with coordinated gene response showed that they suffer a general decompaction upon H1 KD. This is the first report describing simultaneous profiling of five endogenous H1 variants within a cell line and giving functional evidence of genome topology alterations upon H1 KD in human cancer cells.

MATERIALS AND METHODS

Cell lines, culturing conditions and H1 knock-down

Breast cancer T47D-MTVL (carrying one stably integrated copy of luciferase reporter gene driven by the MMTV promoter) derivative cell lines were grown at 37°C with 5% CO2 in RPMI 1640 medium, supplemented with 10% FBS, 2 mM L-glutamine, 100 U/ml penicillin, and 100 μg/ml streptomycin, as described previously (12). HeLa and HCT-116 cell lines were grown at 37°C with 5% CO2 in DMEM GlutaMax medium, supplemented with 10% FBS and 1% penicillin/streptomycin.

T47D-MTVL multiH1sh cell line was used as a model for H1 depletion. This cell line contains a drug-inducible RNA interference system that leads to the combined depletion of H1.2 and H1.4 variants at protein level although it reduces the expression of several H1 transcripts (22). Construction and establishment details of T47D-MTVL multiH1sh cell line are also detailed in 'Materials and Methods' Section of (22). T47D-MTLV H1.0sh, H1.4sh or H1.5sh cell lines contain a drug-inducible RNA interference that specifically deplete the indicated H1 variant. Construction, establishment and validation of these single-H1 knock-downs are reported in (12). To perform experiments, shRNA expression was induced with 6-days treatment of Doxycycline (Dox), in which cells were passaged on day 3. Dox (Sigma) was added at 2.5mg/ml.

Immunoblot

Chromatin samples were exposed to SDS-PAGE (14%), transferred to a PVDF membrane, blocked with Odyssey blocking buffer (LI-COR Biosciences) for 1 h, and incubated with primary antibodies overnight at 4ºC and with secondary antibodies conjugated to fluorescence (IRDye 680 goat anti-rabbit IgG, Li-Cor) for 1 h at room temperature. Bands were visualized in an Odyssey Infrared Imaging System (Li-Cor). Coomassie staining or histone H3 immunoblotting were used as loading controls.

RNA extraction and reverse transcriptase (RT)-qPCR

Total RNA was extracted using the High Pure RNA Isolation Kit (Roche). Then, cDNA was generated from 100 ng of RNA using the Superscript First Strand Synthesis System (Invitrogen). Gene products were analyzed by qPCR, using SYBR Green Master Mix (Invitrogen) and specific oligonucleotides in a Roche 480 Light Cycler machine. Each value was corrected by human GAPDH and represented as relative units. Specific qPCR oligonucleotide sequences are listed in previous studies (22).

Chromatin immunoprecipitation (ChIP)

Chromatin immunoprecipitation was performed according to the Upstate (Millipore) standard protocol. Briefly, cells were fixed using 1% formaldehyde for 10 min at 37ºC, chromatin was extracted and sonicated to generate fragments of 200–500 bp. Then, 30 μg of sheared chromatin was immunoprecipitated overnight with the indicated antibody. Immunocomplexes were recovered using 20 µl of protein A magnetic beads, washed and eluted. Cross-linking was reversed at 65ºC overnight and immunoprecipitated DNA was recovered using the IPure Kit from Diagenode. Genomic regions of interest were identified by real-time PCR (qPCR) using SYBR Green Master Mix (Invitrogen) and specific oligonucleotides in a Roche 480 Light Cycler machine. Each value was corrected by the corresponding input chromatin sample. Oligonucleotide sequences are detailed in previous studies (13).

ChIP-Seq

Library construction and sequencing: Qualified ChIP and Input samples were subjected to end-repair and then 3' adenylated. Adaptors were ligated to the ends of these 3' adenylated fragments. Fragments were PCR-amplified and PCR products were purified and selected with the Agencourt AMPure XP-Medium kit. The double stranded PCR products were heat denatured and circularized by the splint oligo sequence. The single strand circle DNA (ssCir DNA) were formatted as the final library and then quality-checked. The library was amplified to make DNA nanoball (DNB) which had more than 300 copies of one molecular. The DNBs were loaded into the patterned nanoarray and single end 50 bases reads were generated in the way of sequenced by combinatorial Probe-Anchor Synthesis (cPAS).

ChIP-seq data analysis: Single-end reads were quality-checked via FastQC (v0.11.9) and aligned to the human GRCh37/hg19 reference genome using Bowtie2 (v2.3.5.1) (23) with default options. SAMtools (v1.9) (24) utilities were used to filter out the low-quality reads with the flag 3844. Input, H1 variants, and H3K9me3 genome coverage was calculated and normalized by reads per million with BEDTools (v2.28.0) (25), and regions with zero coverage were also reported in the ChIP-Seq annotation (*genomecov -ibam -bga -scale*). MACS2 (v2.1.2) (26) was used to subtract input coverage from H1 variants and H3K9me3 in order to generate signal tracks (*bdgcmp -m subtract*). In the case of H3K9me3 samples, peaks were also called with MACS2 (*callpeak --broad --nomodel --extsize*). SICER (v1.1) was used to identify histone ChIP-enriched regions with the following parameters: redundancy thereshold = 1, window size = 200, fragment size = 150, effective genome fraction = 0.80, gap size = 200 and FDR = 0.01. Genomic annotation of the identified H1-enriched regions was performed with CEAS software.

ChIP-Seq data on histone H1 variants and H3K9me3 epigenetic modification from T47D multiH1sh cells treated or not with Dox has been deposited in NCBI's Gene Expression Omnibus and is accessible through GEO Series accession number GSE156036. ChIP-Seq data on histone H1 variants from WT T47D cells is at GSE166645.

Antibodies

Specific antibodies recognizing human H1 variants used for ChIP/ChIP-seq were: anti-H1.0/H5 clone 3H9 (Millipore, 05-629-I), anti-H1.2 (Abcam, ab4086), anti-H1.4

(Invitrogen, 702876), anti-H1.5 (Invitrogen, 711912) and anti-H1X (Abcam, ab31972). ChIP-seq of H3K9me3 was performed using anti-H3K9me3 (Abcam, ab8898). Other antibodies used were: anti-H1.0 (Abcam, ab11079), anti-H1.3 (Abcam, ab24174), anti-H1.5 (Abcam, ab24175), H1-T146p (ab3596) and anti-H3 (Abcam, ab1791).

In situ Hi-C analysis

Hi-C libraries were generated from T47D multiH1sh cells treated or not with Dox, in duplicate, as previously described (27, 28). In brief, adherent cells were cross-linked with 1% formaldehyde in PBS for 10 min at room temperature and glycine 0.125 M was added for 5 min at room temperature and for 15 min at 4ºC to stop the cross-link reaction. Before permeabilization, cells were treated for 5 min with trypsin. Nuclei digestion was performed with 400 units of MboI restriction enzyme. The ends of restriction fragments were labeled using biotinylated nucleotides and ligated with T4 DNA ligase. After reversal of cross-links, DNA was purified and sheared (Diagenode BioruptorPico) to obtain 300-500 bp fragments and ligation junctions were pull-down with streptavidin beads. Hi-C libraries were finally amplified, controlled for quality and sequenced on an Illumina HiSeq 2500 sequencer.

Hi-C data pre-processing, normalization and generation of interaction matrices

The analysis of Hi-C data, from FASTQ files mapping to genome segmentation into A/B compartments and TADs, was performed using TADbit (29), which started by performing a quality control on the raw data in FASTQ format. Next, sequencing reads were mapped to the reference genome (GRCh37/hg19) applying an iterative strategy and using the GEM mapper (30). Mapped reads were filtered to remove those resulting from unspecified ligations, errors or experimental artefacts. Specifically, nine different filters were applied using the default parameters in TADbit: self-circles, dangling ends, errors, extra dangling-ends, over-represented, too short, too long, duplicated and random breaks (29). Hi-C data were next normalized with ICE Vanilla correction (31) at the resolutions of 1 Mb, 500 kb, 100 kb and 10 kb, to remove Hi-C biases and artifacts. Filtered read-pairs were binned at the resolutions of 1 Mb, 500 kb, 100 kb and 10 kb, applying biases from the normalization step and decay correction to generate interaction matrices. Hi-C data on T47D breast cancer cells has been deposited in NCBI's Gene Expression Omnibus and is accessible through accession number GSE147627. A summary of the number of valid reads obtained per replica and filtered artifacts is shown as Supplementary Table 1.

Genome segmentation into Topologically Associating Domains (TADs)

We identified TADs at the resolution of 50kb using TADbit with default parameters. TADbit segments the genome into constitutive TADs after analyzing contact distribution along the genome. TADbit employs a BIC-penalized breakpoint detection algorithm based on probabilistic interaction frequency model, that returns the optimal segmentation of the chromosome (6). This algorithm leads to a ~99% average genome coverage. In the output, TADbit also describes TADs border strength and TADs density. TADs border strength is the algorithm likelihood corresponding to each border (the higher the strength, the higher the algorithm confidence). To assign a strength value, TADbit repeats the dynamic programming segmentation 10 times after the optimum is reached, each time adding a TAD border. The strength of a TAD border is the number of times it was included in the optimal segmentation, and it thus ranges from 1 to 10 (32). TADs density is the number of interactions within each TAD compared to the others (the higher the density, the higher the number of interactions within the TAD).

Genome segmentation into A/B compartments

We segmented the genome into A/B compartments at 100kb resolution using HOMER software (33). Briefly, HOMER calculates correlation between the contact profiles of each bin against each other, and performs principal component analysis (PCA) on chromosome-wide matrices. Normally, A compartment is assigned to genomic bins with positive first principal component (PC1), and B compartment is assigned to genomic bins with negative PC1. However, in some cases PC1 is reversed in the sign, with A compartment actually corresponding to negative PC1, and B compartment corresponding to positive PC1. Also, it might happen that PC1 captures the two chromosomal arms and that PC2 must be used to identify compartments. For these reasons, GC-content profile was used as a probe for A compartments. For each chromosome, PC1 and PC2 were inspected and compared to GC-content profile to correctly assign compartments.

Gene Ontology analysis of genes located within bins showing compartment shift was performed using Molecular Signatures Database (MsigDB), a collection of gene sets for use with Gene Set Enrichment Analysis (GSEA) software.

3D modelling of TADs based on Hi-C data

We used TADbit to generate 3D models of selected TADs at the resolution of 10 kb (29). Hi-C interaction maps were transformed into a set of spatial restraints that were then used to build 3D models of the TADs that satisfied as best as possible the imposed restraints, as previously described (34)(35). For each TAD, we generated 1,000 models, structurally aligned and clustered them in an unsupervised manner, to generate sets of structurally related models. For every TAD, we used the main cluster to compute consistency, accessibility, density, interactions, radius of gyration, and walking angle (35). Consistency quantifies the variability of the position of particles across the considered set of models. Accessibility measures with a fraction from 0 to 1 how much models are accessible to an object (*i.e.* a protein) with a radius of 100 nm. Density expresses local compactness and is the ratio of bin size (in base pairs) and distances between consecutive particles in the models – the higher the density, the more compact the DNA. Interactions represent the number of particles closer than a cut-off of 200 nm. Radius of gyration indicates 3D structure compactness around its center of mass. Finally, walking angle measures the angle between triplets of consecutive particles – the higher the value, the straighter the models.

ATAC-Seq data analysis

ATAC-Seq data identified by the accession number GSE100762 was reprocessed as described (36) with slight modifications. Paired-end reads were quality-checked via FASTQC (v0.11.9), trimmed, and subsequently aligned to the human GRCh37/hg19 reference genome using Bowtie2 (v2.3.5.1). SAMtools (v1.9) was used to filter out the low-quality reads with the flag 1796, remove reads mapped in the mitochondrial chromosome and discard those with a MAPQ score below 30. The peak calling was performed with MACS2 (v.2.1.2) by specifying the *-BAMPE* mode. Filtered BAM files were also used to compute the ATAC-Seq genome coverage, which was normalized by reads per million (*genomecov -ibam -bga -scale*).

Genomic data retrieval

Genome-wide GC content, G bands coordinates at 850 bands per haploid sequence (bphs) resolution and chromosomes coordinates were obtained from the UCSC human genome database. G bands average GC content was calculated to subsequently split Gneg bands into four subgroups according to their decreasing GC content. HeLa-S3 genome segmentation by ChromHMM (ENCODE) was obtained from UCSC human genome database.

RESULTS

Genome profiling of five histone H1 variants in breast cancer cells shows differential distribution

We and others have shown that the histone H1 variants content varies between cell types and along differentiation within a particular cell type, and its genomic distribution is non-homogeneous and different between variants. Altering the H1 variants composition in a particular cell type, either artificially or naturally, such as along differentiation or interfering with cell proliferation, may affect the genomic distribution of the different variants. To test this possibility, we took advantage of inducible shRNAs developed to knock-down (KD) human H1 variants. In particular, we performed ChIP-seq experiments in T47D cells harboring an inducible multiH1 shRNA expression vector previously described which, upon Doxycycline treatment, depleted H1.2 and H1.4 proteins efficiently (H1 KD) (22). We prepared chromatin from untreated and 6-days Doxycycline-treated cells and, after testing the efficacy of H1 KD by Western blot (Figure 1A), we performed ChIP with antibodies against endogenous H1.2, H1.4, H1.5, H1.0 and H1X. The amount of DNA immunoprecipitated with H1.2 and H1.4 antibodies decreased >65% in both cases reproducibly among experiments, in treated cells compared to untreated, confirming the antibody specificity on ChIP and the performance of the H1 knock-down. ChIPed DNA was qPCR-amplified with oligonucleotides for TSS and distal promoter regions of *CDK2* (active) and *NANOG* (inactive) genes (Figure 1B). This showed that all ChIPs worked efficiently compared to unspecific IgG. The active gene presented the characteristic H1 valley at TSS compared to the distal region, but not the inactive gene (18). Upon H1 KD, H1.2 and H1.4 signal decreased importantly, while H1.0 signal was increased, in agreement with its increase observed by Western blot (Figure 1A-B). The specificity of H1 antibodies not used before was further tested on Western blot and ChIP-qPCR with chromatin extracts from HeLa and HCT-116 cells, which lack H1.0 or H1.5, respectively, and with chromatin extracts from H1.0, H1.4 or H1.5 single KD T47D cells (Suppl. Figure 1A-D). Further, the effect of H1 KD was confirmed by RT-qPCR, showing inhibition of multiple H1 variant genes and induction of satellites, repeats and interferon stimulated genes (ISGs) (Suppl. Figure 1E).

We have previously shown that quantification of the average abundance of each H1 variant input-subtracted ChIP-seq signal at cytobands (G bands) is an efficient method to compare their distribution (20). G bands were classified as G positive (Gpos25 to Gpos100, according to its intensity upon Giemsa staining), and G negative (unstained), which were further divided into four groups according to their GC content (Gneg1 to Gneg4, from high to low GC content) (Figure 1C). We calculated the abundance of each H1 within the G bands to compare its distribution upon H1 KD. In the absence of Dox, H1.2 was seen enriched towards low GC (Gpos100/Gneg4, repressed) bands, and H1X was enriched at high GC (Gpos25/Gneg1, active) bands, as expected from previous studies (18, 20). Besides, H1.4 was also enriched at high GC bands, whereas H1.5 and H1.0 were enriched towards low GC bands (Figure 1C).

When plotted H1.2 abundance against H1X, either within G bands or within 100-kb bins, a negative correlation was observed (Figure 1D and Suppl. Figure 2B). Besides, H1.2, H1.5 and H1.0 strongly correlated within 100-kb bins, indicating that these three variants occupy the same genomic regions in T47D cells, being more abundant within low GC regions (Figure 1D and Suppl. Figure 2A). H1.4 and H1X also correlated, especially at low GC bins, being H1X more abundant than H1.4 at high GC regions. As a consequence, two groups of variants were established, being H1.2 and H1X the prototypes of the two groups, with opposed distribution within the genome. The ratio between these two variants at each G band was calculated. The H1.2/H1X ratio was higher not only at low GC Gpos and Gneg bands, but also at low GC content chromosomes (Suppl. Figure 2C-E). These are chromosomes with a lower gene richness and average gene expression (18).

Depletion of multiple histone H1 variants results in a small redistribution of remaining variants

Upon Dox treatment, H1.2 and H1.4 were strongly depleted but still immunoprecipitated (Figure 1B); while H1.2 relative distribution was not significantly changed, H1.4 enrichment at high GC bands was lost (Figure 1C). Upon H1 depletion, H1X increased its enrichment at high GC bands and decreased at low GC bands (Figure 1C). Instead, H1.0 and H1.5 relative distributions were almost unaltered upon H1 KD.

Changes of H1 variants distribution upon H1 KD were further analyzed within 100-kb bins throughout the genome (Figure 1E). Scatter plots confirmed that H1.0 distribution was completely unaltered, while H1.2 and H1.5 were slightly increased at high GC regions. As indicated, H1X was highly enriched at high GC bins and decreased at low GC bins, whereas H1.4 was decreased from high GC regions. By analyzing the H1 content within 100-kb bins of each chromosome, we observed that upon H1 KD, H1X increased its relative abundance within high GC, low H1.2/H1X ratio chromosomes (Suppl. Figure 2F). Instead, H1.4 decreased drastically its abundance within these chromosomes. H1.2 and H1.5 also slightly increased their relative abundance within high GC chromosomes, whereas H1.0 was unaltered. A heat map representation of ChIP-seq data of all H1 variants abundance within G bands from different experiments confirmed the formation of two clusters representing the two H1 variant profiles (Suppl. Figure 2G).

The average profiles of all H1 variants around transcription start sites (TSS) or termination sites (TTS) and around coding genes was calculated using CEAS software and is shown in Supplementary Figure 3A. All H1 variants showed depletion around TSS of active genes and no changes upon H1 KD, except for H1X, which was enriched around TSS of genes, especially upon H1 KD, parallel to its enrichment at high GC regions, in agreement with previous data on wild-type T47D cells (18). Annotation of genomic regions enriched for the different variants showed that H1.2, H1.5 and H1.0 were enriched at intergenic regions both in the absence or presence of Doxycycline, whereas H1X and H1.4 were enriched at promoters and introns in wild-type conditions, but distribution was altered upon H1 KD (Suppl. Figure 3B). H1X was further enriched at promoters, exons and UTRs, whereas H1.4 was decreased from introns and increased at intergenic regions.

In summary, ChIP-seq data in T47D cells demonstrated that H1 variants are differentially distributed through the genome in two profiles: H1.2, H1.5 and H1.0 enriched towards low GC regions whereas H1X and H1.4 more abundant at high GC regions. Upon H1.2 and H1.4 depletion, H1.2, H1.0 and H1.5 did not change much their relative abundance among high or low GC bands, whereas H1X enhanced its abundance at high GC regions, where H1.4 was selectively depleted. H1.0, whose expression and protein levels were increased trying to compensate H1 levels, was incorporated homogeneously throughout the genome.

Profiling of H1 variants within chromatin states

Using multiple genomic data such as ChIP-seq of core histone modifications and chromatin proteins, FAIRE-seq and DNase-seq, up to 10 chromatin states or 'colors' have been established for several human cell lines (37). Because this data is not available for T47D cells, we calculated the abundance of H1 variants profiled in T47D cells within the genomic coordinates of HeLa-S3 chromatin states as an approximation and represented the data as a heat map (Figure 1F). ChIP-seq data of H3K9me3 profiled in parallel to H1 variants was also represented. This analysis showed that H1s are particularly abundant within *heterochromatin/repetitive* and *low-activity* chromatin states, but also at *polycomb-repressed*, *transcription-associated* and *weak-enhancer*. H1s were underrepresented at *active* and *inactive promoter* states. This was true for all H1 variants, except H1X, but including H1.4. A similar profile was observed for H3K9me3, which was almost identical to H1.4 profile. H1X was more abundant at *promoters*. Clustering confirmed that H1X is the most distant variant, and H1.4 presented an intermediate profile. Upon H1 KD (Dox treatment), H1.2, H1.5 and H1.0 profiles within chromatin states were not altered. H1.4 profile was slightly switched towards the H1.2 cluster. Instead, H1X profile was pronouncedly affected; H1X was decreased at *heterochromatin* and increased in almost all other chromatin states, particularly at *polycomb-repressed* regions and *promoters*, and among them the highest increase occurred at *inactive promoters* (Figure 1F and Suppl. Figure 3C).

Because this clustering analysis was based on the mean H1 variant abundance within each chromatin type and each type represents very different proportions and fragment sizes of the genome (Suppl. Figure 3D), a heat map using 1,000 randomly-picked fragments of each type was represented (Suppl. Figure 3E). Clustering confirmed that H1X was the most extreme variant and H1.4 showed an intermediate distribution together with H3K9me3.

In order to relate G banding and chromatin colors, as this has not been done before to our knowledge, an overlap analysis was performed (Suppl. Figure 3F,G). As predicted, low GC bands were highly enriched in heterochromatin, whereas all chromatin types related to promoters, enhancers and transcription, including Polycomb-repressed, were enriched at high GC bands. Distal CTCF/candidate insulator and low-activity colors were distributed homogenously among all G bands.

Depletion of multiple histone H1 variants in breast cancer cells promotes changes on genome architecture

i) Location of TADs and A/B compartments in T47D multiH1 KD cells

Chromosome conformation capture techniques such as Hi-C allows to detect local and distal contacts within the genome and to establish the position of borders flanking the so-called topologically associating domains (TADs). Hi-C experiments also allow to establish a division of the genome into two compartments, active (A) and inactive (B). To address the consequences of histone H1 depletion on genome architecture, we prepared nuclear DNA from untreated and 6-days Doxycycline-treated multiH1 KD cells, in duplicate, and performed the Hi-C protocol. From the interactions map we calculated the position of TADs within the genome as well as the location of A and B compartments (Suppl. Figure 4). The identity of A and B compartments was established from the principal component (PC1) values. We have previously shown that T47D A compartment corresponds to high-GC bands, early-replicating, accessible chromatin, and B compartment coincides with low-GC bands, late-replicating, inaccessible regions (20). When overlapped with the chromatin states, the B compartment of the genome was enriched in heterochromatin while the A compartment was enriched in transcription-related chromatin states, as expected (Suppl. Figure 3F,G). Furthermore, we calculated the abundance of H1.2 and H1X within TADs, as well as the H1.2/H1X ratio for each TAD, and we generated four equivalent groups of TADs from high to low H1.2/H1X (Suppl. Figure 4D). Clusters of TADs with a high H1.2/H1X ratio overlapped considerably well with the B compartment and with low-GC G bands, and the opposite occurred for the low H1.2/H1X-ratio TADs.

ii) Transitions between A/B compartments at regions enriched in H1.2

Next, we analyzed whether upon H1 depletion the number and position of compartments and TADs was altered. The identity of A and B compartments was mostly preserved compared to untreated cells, with about 3.0% of 100-Kb bins or regions changing from B to A (decompaction) and 3.2% changing from A to B (compaction), globally, upon H1 depletion (Figure 2A). These changes were not homogeneous among chromosomes. A-to-B and B-to-A shifts upon H1 KD occurred more frequently within chromosomes enriched in H1.2 (high average H1.2/H1X ratio within TADs) and that presented the highest proportion of bins within the B compartment and the lowest within the A compartment (Figure 2B). Notably, the negative correlation existing between H1.2/H1X ratio and the % of bins in A was lost in bins changing from A to B.

In addition to A-to-B and B-to-A shifts, changes in PC1 values within compartments corresponding to compaction or decompaction upon H1 KD were also considered (Figure 2A,C). A total of 2,882 100-kb bins (7.3%) were compacted and 2,565 bins (6.3%) were decompacted, while 21,899 bins (80%) remained unchanged. The proportion of bins within A or B compartment was 50% for both.

RNA-seq data on multi H1 KD cells treated or not with Dox to induce shRNA expression was available from previous work (GEO accession number GSE83277) (22). We explored whether gene expression (normalized RNA-seq reads) was altered within bins changing compaction upon H1 KD (Figure 2D). Significant overall gene up-regulation was observed within bins being decompacted (B-to-A and A decompaction), but not within bins being compacted. Considering a gene expression fold-change ≥1.4 and *P*-value<0.05, 73 genes were up-regulated and 44 down-regulated within bins decompacted upon H1 KD. Within bins being compacted, 97 genes were up- and 138 genes were down-regulated. Besides, many up- or down-regulated genes upon H1 KD were located within bins not changing compartment identity or compaction. As expected, many more genes were located within A compartment than in B. Genes in A compartment were down-regulated in a larger proportion than up-regulated (898 vs. 642 genes, considering FC≥1.4). Within B compartment 133 genes were up-regulated and 84 genes down-regulated. In conclusion, gene up-regulation was mainly observed within bins located in B compartment or that became decompacted upon H1 KD. Nevertheless, and somehow unexpected, gene down-regulation also occurred, mainly within A compartment and at regions being compacted.

The representation in scatter plots of the PC1 from untreated cells against the H1 content within individual 100kb bins showed that H1.2 correlated negatively with PC1 whereas H1X correlated positively (Figure 2E). Interestingly, a population of bins extruded from the general trend. These were bins with weak A compartment strength, less H1.2 and more H1X than expected, which were enriched in A decompaction bins (1,508 bins; A unchanged 84.7%, A decompaction 12.4%, A compaction 1.8%, A-to-B 1%). This subset of bins was highly enriched in chromatin states related to active transcription and devoid of heterochromatin, compared to the chromatin states composition of other A compartment groups (Figure 2E,F). The chromatin states composition of each bin category showed that all groups in the B compartment in WT cells were enriched in heterochromatin compared to groups in the A compartment, although differences between groups existed (Figure 2F). The A-decompaction group was enriched in *yellow* (weak enhancer) and *black* (Polycomb-repressed) chromatin colors, and the B-decompaction was the most heterochromatic group of all. The reported association of H1 with Polycomb and heterochromatin proteins could explain the decompaction of A and B-associated regions enriched in these chromatin types.

The H1 variants content in all bin groups described in Figure 2C was calculated using the ChIP-seq data of untreated cells (wild-type). H1.2, H1.5 and H1.0 were more abundant at B compartment bins than A, while H1.4 and H1X were more abundant at A compartment (Figure 2G). Bins changing from B to A were not as rich in H1.2 as bins in B, but still richer than A or A-to-B bins, and they were poor in H1X and H1.4. On the other hand, bins A-to-B were richer in H1.2 and poorer in H1.X than A bins. Altogether, the data suggests that compartment changes (A-to-B and B-to-A) upon H1 depletion were occurring in regions initially enriched in H1.2 or poor in H1X (high 2/X ratio). All groups presenting changes in compaction within or among compartments presented more H1.2, H1.5 and H1.0 and less H1X and H1.4 than the unchanged A compartment bins.

Upon H1 KD, in bins changing from B to A, compared to B (unchanged) bins, all H1 variants were decreased, except H1X, in agreement with chromatin opening. Within bins changing from A to B, compared to A bins, H1.2, H1.5 and H1X were decreased, while H1.4 and H1.0 were increased (Figure 2H). Overall, H1.2 was depleted more pronouncedly from bins that changed compartment than from bins that maintained its compartment identity, which suggests that H1.2 depletion caused the compartment shifts. Interestingly, H1.0 changes within bin groups were slightly different than H1.2 and H1.5. Besides, H1.0 was increased within B groups and reduced within A groups, suggesting that upon H1 KD the overall increase in H1.0 expression was used to replenish the B compartment. Similarly, despite H1.4 depletion, this variant decreased from all A compartment groups but increased at B groups. Instead, H1X was further increased at A unchanged and A decompacted bins, and decreased from all B groups and compacted bins (Figure 2H).

iii) Changes in TAD borders location and strength

Further, TAD analysis showed that TADs number was slightly changed upon H1 depletion (3,009 -Dox vs. 2,718 +Dox) (Figure 3A,B and Suppl. Figure 4D). The number of TAD borders within A compartment decreased ca. 15.16% upon H1 KD (from 1,925 to 1,633), while the number of borders located at the B compartment remained unaltered (1,055). This could be due either to shifts in TAD borders, or to shifts in A/B compartments as shown in Figure 2. There were more TAD borders within the A compartment than in B, indicating that TADs are shorter at the A compartment. Upon H1 KD, the number of TAD borders in A was reduced and, consequently, some TADs increased its length. Approximately 71% of TAD borders detected in untreated cells were unchanged upon H1 knock-down, and another 12.4% of the borders (N=373) were found shifted by only one bin (that is. 100 Kb). Finally, 16.5% of the borders were not conserved; shifted by ≥2 100-kb bins, or disappeared (-Dox, N=498; +Dox, N=207). Conserved borders were located similarly within the A and B compartments (Figure 3C). Shifted borders were enriched at the B compartment, whereas non-conserved borders were enriched within A, and after H1 KD these borders were homogeneously distributed between A and B compartments, probably related to the decrease of borders within A reported above (Figure 3C).

To determine whether those changes could be linked to the H1 depletion, we interrogated if the non-conserved borders were located within H1.2 or H1.4 enriched TADs. H1.2 abundance was significantly lower at non-conserved compared to conserved borders (Figure 3D). Instead, H1.4 was higher at TADs with shifted or non-conserved borders. This suggested that TADs that changed their borders upon H1 KD were poor in H1.2 and rich in H1.4, as occurs at the A compartment.

Next, we calculated the border strength of each TAD border, expressed on a scale of 1 (low) to 10 (high) as reported by TADbit (29). The number of TAD borders with maximal strength was decreased from 1,614 to 1,368 (-246, ca. 15.25%) upon H1 KD (Figure 3E). The decrease in the border strength of TADs occurred at conserved, shifted and non-conserved TAD borders (Figure 3F). Notably, border strength was higher at conserved borders than shifted or non-conserved borders (Figure 3F), suggesting that soft borders are prone to be altered upon histone H1 depletion, both in its position as well as in its strength. Upon H1 depletion, TAD border strength was decreased at A compartment, but not much at B compartment (Figure 3G), in agreement with the decrease of borders within this compartment.

iv) Changes in short- and long-range contacts

Analysis of genomic Hi-C interactions as a function of genomic distance showed that H1 depletion decreased short- and medium-range interactions (up to ~30 Mb) (Figure 4A). Longer-range contacts (>50 Mb) were increased upon H1 loss. These distinct effects were also observed in matrices that represented gained and lost interactions along a chromosome in H1 depleted cells relative to control cells (Figure 4B). Knock-down of H1 variants decreased intra-TAD, very short-range interactions, especially within the A compartment, in line with a decrease in TAD border strength, but also within B compartment and between A-B compartments (Figure 4C). H1 depletion also decreased inter-TAD, medium-range interactions, both within A and B compartments and in less proportion between TADs located in different compartments (Figure 4C). In conclusion, combined depletion of H1.2 and H1.4 altered chromatin conformation at both B and A compartments, as these H1 variants occupy opposed genomic regions. These data suggest that H1 proteins are fundamental to maintain TAD structure.

v) Changes in ATAC-seq signal and H3K9me3 distribution

In parallel, ATAC-seq accessibility was significantly increased at both A and B compartments upon H1 depletion (Figure 4D). Upon H1 depletion, accessibility was significantly increased at all TADs categories, but was higher at low H1.2/H1X TADs (Figure 4E). Accordingly, accessibility was also increased the most within high GC cytobands upon H1 KD (Suppl. Figure 5A). Not only ATAC-seq peaks count was increased upon H1 KD, but also ATAC-seq reads signal within peaks that were conserved between –Dox/+Dox (Suppl. Figure 5B).

ChIP-seq of the repressive mark H3K9me3 upon H1 KD was also performed. As expected, in untreated cells, this mark was accumulated at gene-poor, low GC bands (Suppl. Figure 5C) and at the B compartment (Figure 4F). Upon H1 KD, H3K9me3 ChIP-seq signal was decreased more importantly from the high GC bands, from A compartment, and from low H1.2/H1X TADs (Figure 4F), as if chromatin decompaction occurred more importantly at already open regions, as also shown by ATAC-seq. Moreover, in untreated cells, peak calling gave 64,585 broad peaks of H3K9me3 enrichment, more abundant at low GC regions, whereas upon H1 KD the number of peaks was reduced to 1,044 (restricted to 173 bands, 22% of total cytobands), indicating that H3K9me3 signal was diffused upon H1 KD (Suppl. Figure 5D). H3K9me3 peaks retained in H1 KD cells were at low GC, compacted regions, enriched in LINEs compared to SINEs/Alus (Suppl. Figure 5E).

Overall, we have shown that upon H1 KD, active/open regions with a lower relative content of H1.2 (A compartment, high-GC cytobands, TADs with low H1.2/H1X ratio) became even more accessible compared to inactive/closed regions, with a higher loss of H3K9me3. Moreover, those TADs decreased intra- and inter-TAD contacts. Within inactive/closed regions (B compartment), with a high H1.2/H1X ratio, contacts were also decreased upon H1 KD, but to a minor extent. Accessibility was poorly increased and H3K9me3 signal was conserved, although its distribution was broader (less peaks were detected).

Relation between changes in gene expression and changes within TADs upon H1 depletion

i) Distribution of genes deregulated upon H1 depletion within TADs

Multiple H1 depletion caused up-regulation of 1,089 genes and down-regulation of 1,254 genes (FC ≥ 1.4, adjusted *P*-value ≤ 0.05). As previously shown (22), about 36% of up-regulated genes are related to the transcriptional response to interferon (Figure 5A). We interrogated whether some of these genes were co-localized within the same TADs and whether these TADs have any common features. A total of 2,291 deregulated genes (FC≥±1.4) were concentrated within 1,285 TADs (containing from 1 to 34 deregulated genes per TAD), out of 3,009 total TADs (Suppl. Figure 6A). The majority of deregulated genes were alone in a TAD (795 TADs), or in pairs (289 TADs). Other combinatorial coincidences are reported in Supplementary Figure 6A. For instance, there were TADs that concentrated up to 34 de-regulated genes in a same TAD. In addition, TADs containing only up-regulated genes were found to be significantly enriched compared with the expected frequencies obtained after performing 10,000 randomizations of gene locations, while the contrary happened with TADs containing both up- and down-regulated genes ($P<0.01$) (Suppl. Figure 6B). This fact could reflect that these are TADs that may be affected structurally by H1 depletion with specific consequences on gene expression. Alternatively, this could reflect the clustering of interferon-stimulated genes (ISGs) up-regulated upon H1 depletion; as an example, one TAD contains the up-regulated genes IFIT1, IFIT2, IFIT3 and IFIT5. Additionally, the number of de-regulated genes per TAD may be proportional to the total number of genes contained in that TAD. TADs with higher total gene number present higher number of genes deregulated upon H1 depletion (correlation coefficient 0.60, P-value <0.001) (Suppl. Figure 6C).

Focusing on TADs that contained genes exclusively up-regulated (TADS-up, N=516) or down-regulated (TADS-down, N=517) upon H1 depletion (Suppl. Figure 6D), or both up and down-regulated genes within the same TAD (TADS-up&down, N=252), we noticed that TADS-up&down presented the lowest H1.2/H1X ratio and the highest gene richness and average gene expression, followed by TADS-down, TADS-up, and finally TADs without de-regulated genes, which presented the highest H1.2/H1X ratio and the lowest gene richness (Unchanged control, N=1,724) (Figure 5B).

H1.2, H1.5 and H1.0 were more abundant in unchanged TADs, followed by TADS-up, TADS-down and finally TADS-up&down (Figure 5C). Instead, the contrary applied for H1X and H1.4, which were more abundant at TADS-up&down, in agreement with gene richness and GC content. Besides, most of TADs containing significantly deregulated genes upon multiH1 KD were located within the A compartment (Figure 5D). This was more pronounced for TADS-up&down, then TADS-down and, finally, TADS-up, correlating positively with the gene richness, basal gene expression and GC content of these TADs, and negatively with the H1.2/H1X content ratio. TADS without deregulated genes (control) showed the highest presence at B compartment of all TADs. TADs-up overlapped the most with bins shifted from B to A or decompacted within the same compartment upon H1 KD, whereas TADs-down overlapped the most with bins A-to-B or compacted within A (Figure 5D).

When analyzing how the H1 variants were redistributed upon multiH1 KD within these groups of TADs, we observed no big changes in H1.2, H1.5 and H1.0 abundance within any of the TAD groups (Figure 5C). Instead, H1X was significantly enriched within TADS-up&down and depleted from unchanged TADs, without changing its abundance at TADS-up and TADS-down. Finally, H1.4 was depleted the most from TADS-up&down and the least from unchanged TADs and TADS-up.

Further, upon H1 KD, ATAC-seq accessibility was increased globally in all TADs, especially in those containing genes up- and down-regulated simultaneously and with low H1.2/H1X ratio (Figure 5E). Instead, accessibility gain was lower within TADs-up and unchanged TADs. H3K9me3 abundance was decreased in all TADs upon H1 KD, more importantly at TADs-down and TADs-up&down, the contrary that was observed for chromatin accessibility (Figure 5F). Compared to total TADs, changes in intra-TAD interactions upon H1 KD were significantly lower at TADS-up&down only, consequently, no correlation with H1.2/H1X ratio existed (Figure 5G).

Overall, gene expression was not altered (with the criteria FC ≥ 1.4, *P*-value ≤ 0.05) upon H1 KD in most of TADs (53%). These TADS were enriched in H1.2 and contained few genes with low basal expression. TADs containing genes that were up-regulated upon H1 KD only, also presented a low basal gene expression and a high H1.2/H1X ratio. TADs that contained genes up and down-regulated simultaneously were those with a higher gene richness and basal expression, lower H1 ratio, and the highest occupancy within the A compartment. Upon H1 KD, these TADs' chromatin became highly accessible and intra-TAD interactions decreased, parallel to gain in H1X and loss of H1.4.

ii) TADs respond as units to H1 depletion

We have previously reported that shifts on the distribution of H1 variants often coincided with TAD borders and that the distribution of H1 variants (calculated within 100-kb bins) was more homogeneous within the same TAD than between consecutive TADs, randomly picked TADs or randomly defined domains (20). Before using TADs as units to compare the distribution of H1 variants, we have done the same analysis with the ChIP-seq data reported here. Correlation coefficient between the H1 variants analyzed was significantly higher within the same TADs than any other comparison, suggesting that H1 variants were more homogeneous within than between TADs, and that transitions between variants occurred more frequently at the TAD borders (Suppl. Figure 7A). Similarly, the combinations of H1 KD-induced H1 distribution changes were more homogeneous within TADs than either between TADs or within random genomic domains of similar size, indicating that changes are restrained within some TADs (Suppl. Figure 7B). Overall, our results indicate that TADs could act as epigenetic domains, the H1 variants abundance of which can be coordinately modified in response to H1 depletion or changes in the relative abundance of the different variants.

iii) Gene expression is coordinately altered within TADs upon H1 KD

Next, we asked whether the expression pattern of all genes contained within TADs changed coordinately in the same sense upon H1 depletion. For this we calculated whether there was enrichment of TADs with coordinated responses up or down respect to the expected frequency of TADs. The FC limitation to 1.4 was not considered in order to appreciate all changes in gene expression occurring.

Considering TADs with 4 or more genes, the frequency of TADs with increasing proportion of up-regulated (FC > 1) vs. down-regulated genes (FC < -1) upon H1 KD was calculated. For TADs with >70% of up-regulated genes or >80% of down-regulated genes, the observed frequency was higher than the expected frequency (Figure 6A). These correspond to TADs where all or most of the genes changed expression in the same direction upon multiH1 KD; some of the genes were induced with FC≥1.4, including ISGs (Figure 6B-C and Suppl. Figure 8A). This could result from two hypothetical scenarios: i) upon H1 depletion, the whole TADs were (architecturally) affected and all genes became up- or down-regulated coordinately; ii) upon H1 depletion, some gene within a TAD became deregulated (for example, induced ISGs) and, consequently, neighbor genes within the same TAD changed expression in the same sense.

TADs containing all genes co-regulated upon H1 depletion, either down- or up-regulated (groups 0-0.1 and 0.9-1), were poor in gene density, showed low GC content, low basal expression, and high H1.2/H1X ratio (Figure 6D and Suppl. Figure 8B-F). These TADs were enriched in H1.2 and were poor in H1.4 (Suppl. Figure 8G). Upon H1 KD, within these TADs, H1X and H1.4 were slightly decreased, whereas the rest of H1 variants abundances were practically unaltered (Suppl. Figure 8H). In absolute levels, H1.2 and H1.4 were generally depleted (Figure 1A-B). ATAC-seq accessibility increase upon H1 KD was lower within TADs with coordinated response (Figure 6E).

Additionally, these TADs were enriched within the B compartment, whereas TADs containing genes up- and down-regulated simultaneously were enriched within the A compartment (Figure 6F). Noteworthy, TADs with maximal proportion of down- (0-0.1) or up-regulated genes (0.9-1) showed the largest overlap with 100-kb genome segments that shifted from B to A or that were decompacted within the same compartment (Figure 6G), favoring the model that architectural changes due to H1 depletion preceded coordinated changes in gene expression.

In summary, TADs enriched in H1.2 and more repressive, upon H1 KD, harbor more often than expected deregulated genes in the same sense; surprisingly, not only up-regulating gene expression, but also down-regulating genes thereof.

To further characterize TADs according to their activation or repression upon H1 KD in a non-biased way, we ranked TADs containing >3 protein-coding genes according to their global induced changes of expression using the average +Dox/-Dox ratio of the sum of normalized reads per TAD. We subsequently studied the 100 top and bottom TADs (*activated* and *repressed* TADs, respectively) in comparison with the remaining ones (*others*) (Suppl. Figure 9A,B). Activated and repressed TADs presented, respectively, significantly higher and lower average global induced changes of expression compared with the expected distribution of the average values obtained after robustly randomizing the position of the genes (Suppl. Figure 9C). In top and bottom TADs, the expression levels of most protein-coding genes (≈75%) were modified according to the global TAD response (Suppl. Figure 9D). From another point of view, around 57% of TADs classified as activated and repressed showed at least 75% of their protein-coding genes with signs of H1 KD-induced changes coherent with the response at the TAD scale (Suppl. Figure 9E). In addition, the transcribed non-coding regions responded to H1 KD in the same direction as protein-coding genes (Suppl. Figure 9F), suggesting that a global coordinated transcriptional response within responsive TADs was occurring. These results confirm that some TADs respond as a unit to H1 depletion. TADs with the strongest coordinated response to H1 KD activating gene expression were those with a higher H1.2 content and low basal gene expression (Suppl. Figure 9G-L). TADs with the highest abundance of repressed genes showed a higher gene density and H1.4 abundance, and were located at the A compartment. In terms of accessibility gain or H3K9me3 and H1.4 lost, repressed TADs were not much different than the *other* TADs (Suppl. Figure 9G-L).

3D modeling of TADs with coordinated transcriptional response

To further interpret changes in interactions within TADs showing a coordinated transcriptional response to H1 KD in terms of a spatial structure-function relationship, we generated 3D models of genomic regions harboring TADs that contained >90% of genes down or up-regulated (group 0-0.1, *d*, N=36; group 0.9-1, *u*, N=71; Figure 6B), both in WT and H1 KD conditions. Furthermore, we compared the mentioned groups of TADs with the following additional groups: TADs with the most extreme H1.4 decrease upon H1 KD (*h1*, N=100), TADs presenting a bidirectional transcriptional response to multi-H1 KD (*bi*, N=181), TADs presenting the minimum gene expression changes (*mi*, N=100), and TADs without genes (*wi*, N=10). Models were built based on our Hi-C data at 10 kb resolution using TADbit as previously described (Materials and Methods) (29). Several structural measures were computed and compared between groups of modeled TADs, such as: consistency, radius of gyration (a proxy for accessibility), walking angle (measures how straight/stiff the fiber is) (Suppl. Figure 10), and density (indicates compaction) (Figure 7). In untreated cells, all structural measures showed that TADs with the highest H1.4 decrease upon H1 KD (*h1;* rich in H1.4, poor in H1.2 in WT) were significantly different (higher density and walking angle, lower radius of gyration) to the rest of groups. Besides, for several measurements, the group of TADs without genes (*wi)* was also different (lower walking angle) to the other TADs. Upon H1 KD, most of the TAD groups containing genes showed a decrease in density (*h1, bi, ud)* and some of them also in walking angle (*h1, bi*). In general, changes in the structural properties of TADs reflected chromatin relaxation upon H1 KD, such as the significant reduction of chromatin condensation and the destabilization of the DNA fiber conformation, as highlighted by the decrease in density and walking angle within different TADs groups. These changes were more apparent (significant) within TAD groups containing up- and down-regulated genes together (*h1, bi;* or when the up- and down- TADs were pooled; *ud*). Still, although without enough significance, changes in the TADs with a coordinated transcriptional response to H1 KD (*u, d*) went in the same direction, indicating that TADs that were coordinately up- or down-regulated were structurally altered upon H1 KD similarly. In fact, all features shown before for these two groups of TADs were similar (Figure 6 and Suppl. Figure 8). This observation favors the model that all TADs within the genome are altered in a similar way due to H1 KD, with different consequences in gene expression deregulation that might depend on local features or distinct H1 abundance. Furthermore, we discard that changes in TADs structural features are due to gene deregulation going in one or another direction, coordinately or not, as no differences were observed between up- and down-regulated TADs.

DISCUSSION

In this study, we have analyzed the genomic distribution of five endogenous H1 variants within T47D breast cancer cells by ChIP-seq using specific antibodies. This is the whole somatic H1 complement of this cell line with the exception of H1.3 that was not profiled due to the lack of ChIP-grade antibodies, and H1.1 is not expressed in these cells. This is, to our knowledge, the first time that so many endogenous variants have been profiled in a mammalian cell. In previous studies, we mapped endogenous H1.2 and H1X, demonstrating that they have different distributions across the genome (13, 18, 20). On the one side, H1.2 was enriched within intergenic, low gene expression regions and lamina-associated domains (LADs). On the other side, H1X was enriched at gene-rich chromosomes, RNA polymerase II enriched sites, coding regions and hypomethylated CpG islands. Because H1 abundance correlates with high or low GC content, calculating the abundance of H1 variants within G bands is a convenient manner to compare them as we have recently suggested (20). When this method was used, we obtained that H1.5 and H1.0 colocalize with H1.2, at low GC regions, while H1.4 distribution was similar to H1X, although H1X was highly enriched at high GC regions compared to H1.4. Previously, we profiled H1.0 and H1.4 fused to an HA tag at C-termini, stably expressed through a lentiviral vector into T47D cells. In that occasion, both H1.4-HA and H1.0-HA were enriched at high GC regions, indicating that profiling exogenous, tagged H1 proteins may give different results than endogenous proteins (18). On the one hand, endogenous H1.0 has been profiled in human skin fibroblasts, being enriched at high GC regions (19). On the other hand, mouse, tagged, knocked-in H1c (H1.2), H1d (H1.3) and H1.0 have been profiled in ESCs and were found enriched at low GC regions (16). All this together suggests that H1 variants distribution might be different among cell types, and might be related to the relative levels of expression of the different variants. Extensive profiling of H1 variants among different cell types with the same methodology (we favor ChIP-seq of endogenous histones with variant-specific antibodies) should be done to clarify whether distribution of the variants is cell type-specific or universal for some of the variants, parallel to determining the relative H1 content of each cell type analyzed. In T47D cells, the H1 content was estimated to be 9% for H1.0, 23% for H1.2, 13% for H1.3, 24% for H1.4 and 31% for H1.5 (12). This indicates that the major content of H1 is at low GC regions, supporting its role as heterochromatin protein. H1X is thought to be at lower levels and its particular distribution at high GC regions suggests that may play a regulatory role there, as suggested elsewhere (13). The enrichment of H1.4 at high GC regions is intriguing as it was suggested that, because of its K26 residue which may be methylated and bind HP1, it could be related to heterochromatin (38). Still, a fraction of H1.4 is at low GC regions, and even at high GC bands it could have a role in repression at particular sites. In fact, we have found that H1.4 is enriched around peaks of H3K9me3 (Suppl. Figure 11). Additionally, profiling of H1s within chromatin states ('colors') showed that H1.4 profile overlapped H3K9me3 distribution. H1.4 was similar to all variants, enriched at heterochromatin and low-activity chromatin. Instead, H1X was less present at heterochromatin and more abundant at promoters than the others.

To study whether alteration of the total H1 content and relative abundance of the different variants affected the genomic localization of remaining histones, we performed ChIP-seq in T47D cells knocked-down for H1.2 and H1.4 with an inducible system, previously characterized (22). Interestingly, upon H1 KD, H1.4 preferentially remained at low GC regions, supporting its putative role in heterochromatin, and was displaced from high GC regions. In parallel, H1.5 and specially H1X redistributed to high GC regions. H1.0, whose expression and protein levels are increased trying to compensate H1 levels, maintained its distribution. H1.2 was depleted but, in relative terms, it was slightly increased at high GC regions. Profiling within chromatin states showed that H1.4 was slightly switched towards the H1.2 group upon H1 KD, and H1X was decreased at heterochromatin and increased in almost all other chromatin states.

In summary, in the present H1 KD, abundant H1 variants which were preferentially located at high (H1.4) or low (H1.2) GC regions were depleted. As a result, no major redistribution of other variants occurred. Still, the H1 variants selective depletion caused several effects, including changes in gene expression, and derepression of intergenic and intronic RNAs, as well as heterochromatic repeats and ERVs, leading to the induction of the interferon response (22). Moreover, we have shown that H1 KD caused changes in chromatin accessibility and H3K9me3 distribution, shifts in A/B compartments and TAD borders, and changes in the 3D architecture of TADs and of the DNA interactions occurring within and between TADs. Some of these changes were dependent on the compaction or GC content of genomic domains.

We have previously reported that A and B compartments correlate positively with high and low GC content regions, and with TADs presenting a low and high H1.2/H1X ratio, respectively, among other features (20) (Figure 8). The B compartment contains longer TADs, chromatin is more compacted, replicates later than A compartment, gene density and overall gene expression is low, contains repressive histone marks and colocalizes with LADs. We have further described here that these two compartments present different abundance of H1 variants and respond differently to H1 depletion. Upon H1 KD, ATAC-seq chromatin accessibility was increased genome-wide but more importantly at A compartment. The repressive histone mark H3K9me3 was decreased majorly from A compartment, although at B compartment the H3K9me3 signal changed from broad peaks to diffuse signal, pointing to heterochromatin disorganization (Figure 8). Overall genomic architecture was conserved, including partitioning of chromosomes into TADs and compartments. Moreover, we and others have shown that epigenetic states and H1 distribution are more homogeneous within a TAD, suggesting that TAD borders prevent the spreading of these features (6). TADs hardly changed its size or distribution upon multiH1 KD. H1 depletion decreased inter-TAD contacts generally. Instead, TAD border strength and intra-TADs contacts were reduced more predominantly in A compartment. Indeed, several reports have also shown that TAD organization remained largely unchanged when disturbing chromatin homeostasis, including mouse H1-depleted cells or epithelial-to-mesenchymal transition (6, 28, 39, 40). However, in those functional studies, chromatin alteration led to different changes in TAD border strength or intra-TAD interactions, as we have described here as well, reflecting novel chromatin interactions putatively relevant.

Approximately 6% of the genome changed its compartment identity (3.0% from B to A and 3.2% from A to B), correlating with H1.2 enrichment (high H1.2/H1X ratio). Additionally, shifts in the PC1 value (a measure of compartment identity and compaction) within compartments also occurred upon H1 KD. Overall, 9.3% of the genome was decompacted and 10.5% was compacted, including B-to-A and A-to-B shifts. Decompaction associated with gene up-regulation. Recent reports have shown that H1 depletion in mouse T cells and germinal centre (GC) B cells lead to B-to-A compartment shifting mainly (41, 42). These could be due to the fact that differentiated cells present a well-constituted heterochromatin rich in histone H1, compared to pluripotent and cancer cells where chromatin may be more plastic, partially because of a lower H1 content (43, 44). H1-mediated compartmentalization may be established along differentiation, sequestering the stem cell programs within the B compartment. Deregulation of H1 levels and compartmentalization may occur in cancer and along reprogramming (45–47). The observation of A-to-B and B-to-A shifting in our cancer model cells in similar proportions could be due to an overall less compacted chromatin, or to the simultaneous depletion of H1 variants proven here to occupy distinct genomic compartments. In mouse cells, so far only tagged H1c (H1.2) and H1d (H1.3) have been ChIP-seq profiled, showing an overlapping distribution within low GC regions/B compartment (16, 20).

The location of TAD borders within compartments A or B was slightly altered, either due to shifts in TAD borders (ca. 30% of TAD borders were shifted or disappeared), or due to shifts in A/B compartments. Topologically associating domains (TADs) enriched in H1.2 show major changes in interactions and transitions from B to A compartment upon H1 depletion. On the one hand, because H1.2 was abundant at B (low GC) compartment and could be related to gene repression, its depletion in multiH1 KD cells could cause decompaction and B-to-A shifts, accompanied by gene induction and local decrease of DNA interactions. On the other hand, because H1.4 was abundant at A (high GC) compartment and it was depleted preferentially from these regions upon H1 KD, it could cause some A-to-B shifts or compaction, although A decompaction also occurred. H1.4 was similarly enriched (and depleted upon H1 KD) at A compacted and decompacted regions upon H1 KD, suggesting that it might have a dual role that requires further investigation.

Besides, we have shown that responsive genes are non-randomly located throughout the genome but enriched in a limited number of TADs that respond as units in the same sense, up or down, to H1 depletion. We have analyzed TADs that contain genes up- or down-regulated upon H1 KD in three different ways. On the one hand, we considered TADs that contain ≥1 gene with FC≥±1.4, only up- or down-regulated, or containing both up- and down-regulated genes simultaneously. On the other hand, we considered TADs with ≥4 genes where the major part of them (≥80 or ≥90%) are coordinately up- or down-regulated with FC>1. With a third method, we considered the top 100 TADs (with >3 protein-coding genes) presenting the highest overall RNA-seq reads increase or decrease upon H1 KD. With all methods, results were similar, despite TADs considered were not overlapping completely (Suppl. Figure 12). Compared to TADs that contain up- and down-regulated genes simultaneously, TADs that contain only up-regulated genes are rich in H1.2, are more present within the B compartment, present low gene abundance and GC content, and, upon H1 KD, H1X was decreased and H1.4 decreased less than at TADS-up&down (Figure 8). TADs containing only down-regulated genes showed intermediate features. As H1 can be seen as a repressive factor, coordinated gene up-regulation upon H1 KD could be expected. Instead, coordinated down-regulation is more difficult to explain.

We have reported that upon H1 KD in T47D cells the interferon response is induced with many ISGs being up-regulated. This is due to the accumulation of RNAs from repeats and ERVs that stimulate the response at cytoplasm mimicking a viral infection and ending in the transcription of many genes involved in the response. These genes are not activated due to architectural changes promoted by H1 depletion from chromatin. Instead, other genes not related to such response may be deregulated due to structural changes, chromatin decompaction, TAD border alterations or changes in the short- or long-distance interactions. We have found ISGs up-regulated within TADs with a coordinated response to H1 KD. As the FC of ISGs is often higher than that of other genes within the same TAD, we cannot discard that those changes are somehow related to the induction of ISGs. Importantly, most of TADs with a coordinated response do not contain ISGs, so we favor that the response may be a consequence of architectural changes. Altogether, our results support H1 variants heterogeneity as well as their key role in the topological organization of the genome that has consequences on gene expression programs.

ACCESSION NUMBERS

Hi-C and ChIP-seq data on T47D breast cancer cells reported here and deposited in NCBI's Gene Expression Omnibus are accessible through GEO Series accession number GSE147627 and GSE156036/GSE166645, respectively.

SUPPLEMENTARY DATA

Supplementary Table 1 and Figures 1 to 12 are available online.

ACKNOWLEDGEMENTS

We acknowledge Generalitat de Catalunya and the European Social Fund for AGAUR-FI predoctoral fellowships [to M.S.-P. and to F.M.].

FUNDING

This work was supported by the Spanish Ministry of Science and Innovation [BFU2017-82805-C2-1-P to A.J., BFU2017-85926-P to M.A.M-R.(AEI/FEDER, UE)]. This research was partially funded by the European Union's Seventh Framework Programme the ERC grant agreement 609989 to M.A.M-R., European Union's Horizon 2020 research and innovation programme grant agreement 676556 to M.A.M-R. We also acknowledge the Generalitat de Catalunya Suport Grups de Recerca AGAUR 2017-SGR-597 to A.J. and 2017-SGR-468 to M.A.M-R. CRG acknowledges support from 'Centro de Excelencia Severo Ochoa 2013-2017', SEV-2012-0208 and the CERCA Programme/Generalitat de Catalunya as well as support of the Spanish Ministry of Science and Innovation through the Instituto de Salud Carlos III, the Generalitat de Catalunya through Departament de Salut and Departament d'Empresa i Coneixement, and the Co-financing by the Spanish Ministry of Science and Innovation with funds from the European Regional Development Fund (ERDF) corresponding to the 2014-2020 Smart Growth Operating Program. Funding for open access charge: Spanish Ministry of Science and Innovation.

CONFLICT OF INTEREST

No conflict of interest needs to be reported.

REFERENCES

1. Lieberman-Aiden,E., Van Berkum,N.L., Williams,L., Imakaev,M., Ragoczy,T., Telling,A., Amit,I., Lajoie,B.R., Sabo,P.J., Dorschner,M.O., *et al.* (2009) Comprehensive mapping of long-range interactions reveals folding principles of the human genome. *Science (80-.).*, **326**, 289–293.
2. Dixon,J.R., Selvaraj,S., Yue,F., Kim,A., Li,Y., Shen,Y., Hu,M., Liu,J.S. and Ren,B. (2012) Topological domains in mammalian genomes identified by analysis of chromatin interactions. *Nature*, **485**, 376–380.
3. Nora,E.P., Lajoie,B.R., Schulz,E.G., Giorgetti,L., Okamoto,I., Servant,N., Piolot,T., Van Berkum,N.L., Meisig,J., Sedat,J., *et al.* (2012) Spatial partitioning of the regulatory landscape of the X-inactivation centre. *Nature*, **485**, 381–385.
4. Sexton,T., Yaffe,E., Kenigsberg,E., Bantignies,F., Leblanc,B., Hoichman,M., Parrinello,H., Tanay,A. and Cavalli,G. (2012) Three-dimensional folding and functional organization principles of the Drosophila genome. *Cell*, **148**, 458–472.
5. Rao,S.S.P., Huntley,M.H., Durand,N.C., Stamenova,E.K., Bochkov,I.D., Robinson,J.T., Sanborn,A.L., Machol,I., Omer,A.D., Lander,E.S., *et al.* (2014) A 3D map of the human genome at kilobase resolution reveals principles of chromatin looping. *Cell*, 10.1016/j.cell.2014.11.021.
6. Le Dily,F.L., Baù,D., Pohl,A., Vicent,G.P., Serra,F., Soronellas,D., Castellano,G., Wright,R.H.G., Ballare,C., Filion,G., *et al.* (2014) Distinct structural transitions of chromatin topological domains correlate with coordinated hormone-induced gene regulation. *Genes Dev.*, **28**, 2151–62.
7. Bednar,J., Horowitz,R.A., Grigoryev,S.A., Carruthers,L.M., Hansen,J.C., Koster,A.J. and Woodcock,C.L. (1998) Nucleosomes, linker DNA, and linker histone form a unique structural motif that directs the higher-order folding and compaction of chromatin. *Proc Natl Acad Sci U S A*, **95**, 14173–14178.
8. Millán-Ariño,L., Izquierdo-Bouldstridge,A. and Jordan,A. (2016) Specificities and genomic distribution of somatic mammalian histone H1 subtypes. *Biochim. Biophys. Acta - Gene Regul. Mech.*, **1859**, 510–519.
9. Fyodorov,D. V, Zhou,B.-R., Skoultchi,A.I. and Bai,Y. (2018) Emerging roles of linker histones in regulating chromatin structure and function. *Nat. Rev. Mol. Cell Biol.*, **19**, 192–206.
10. Izzo,A., Kamieniarz,K. and Schneider,R. (2008) The histone H1 family: specific members, specific functions? *Biol. Chem.*, **389**, 333–343.
11. Happel,N. and Doenecke,D. (2009) Histone H1 and its isoforms: Contribution to chromatin structure and function. *Gene*, **431**, 1–12.
12. Sancho,M., Diani,E., Beato,M. and Jordan,A. (2008) Depletion of human histone H1 variants uncovers specific roles in gene expression and cell growth. *PLoS Genet.*,

4, e1000227.

13. Mayor,R., Izquierdo-Bouldstridge,A., Millán-Ariño,L., Bustillos,A., Sampaio,C., Luque,N. and Jordan,A. (2015) Genome distribution of replication-independent histone H1 variants shows H1.0 associated with nucleolar domains and H1X associated with RNA polymerase II-enriched regions. *J. Biol. Chem.*, **290**, 7474–91.
14. Kalashnikova,A.A., Winkler,D.D., McBryant,S.J., Henderson,R.K., Herman,J.A., DeLuca,J.G., Luger,K., Prenni,J.E. and Hansen,J.C. (2013) Linker histone H1.0 interacts with an extensive network of proteins found in the nucleolus. *Nucleic Acids Res.*, **41**, 4026–4035.
15. Li,J.Y., Patterson,M., Mikkola,H.K.A., Lowry,W.E. and Kurdistani,S.K. (2012) Dynamic Distribution of Linker Histone H1.5 in Cellular Differentiation. *PLoS Genet.*, **8**, e1002879.
16. Cao,K., Lailler,N., Zhang,Y., Kumar,A., Uppal,K., Liu,Z., Lee,E.K., Wu,H., Medrzycki,M., Pan,C., *et al.* (2013) High-resolution mapping of H1 linker histone variants in embryonic stem cells. *PLoS Genet.*, **9**, e1003417.
17. Izzo,A., Kamieniarz-Gdula,K., Ramírez,F., Noureen,N., Kind,J., Manke,T., van Steensel,B. and Schneider,R. (2013) The genomic landscape of the somatic linker histone subtypes H1.1 to H1.5 in human cells. *Cell Rep.*, **3**, 2142–54.
18. Millán-Ariño,L., Islam,A.B.M.M.K., Izquierdo-Bouldstridge,A., Mayor,R., Terme,J.M., Luque,N., Sancho,M., López-Bigas,N. and Jordan,A. (2014) Mapping of six somatic linker histone H1 variants in human breast cancer cells uncovers specific features of H1.2. *Nucleic Acids Res.*, **42**, 4474–4493.
19. Torres,C.M., Biran,A., Burney,M.J., Patel,H., Henser-Brownhill,T., Cohen,A.H.S., Li,Y., Ben-Hamo,R., Nye,E., Spencer-Dene,B., *et al.* (2016) The linker histone H1.0 generates epigenetic and functional intratumor heterogeneity. *Science (80-.).*, **353**, aaf1644.
20. Serna-Pujol,N., Salinas-Pena,M., Mugianesi,F., Lopez-Anguita,N.,Torrent-Llagostera,F.,Izquierdo-Bouldstridge,A.,Marti-Renom,MA.,Jordan,A. (2020) TADs enriched in histone H1.2 strongly overlap with the B compartment, inaccessible chromatin and AT-rich Giemsa bands. *FEBS J.*, 10.1111/febs.15549.
21. Geeven,G., Zhu,Y., Kim,B.J., Bartholdy,B.A., Yang,S.M., Macfarlan,T.S., Gifford,W.D., Pfaff,S.L., Verstegen,M.J.A.M., Pinto,H., *et al.* (2015) Local compartment changes and regulatory landscape alterations in histone H1-depleted cells. *Genome Biol.*, 10.1186/s13059-015-0857-0.
22. Izquierdo-Bouldstridge,A., Bustillos,A., Bonet-Costa,C., Aribau-Miralbés,P., García-Gomis,D., Dabad,M., Esteve-Codina,A., Pascual-Reguant,L., Peiró,S., Esteller,M., *et al.* (2017) Histone H1 depletion triggers an interferon response in cancer cells via activation of heterochromatic repeats. *Nucleic Acids Res.*, **45**, 11622–11642.
23. Langmead,B. and Salzberg,S.L. (2012) Fast gapped-read alignment with Bowtie 2.

Nat. Methods, **9**, 357–359.

24. Li,H., Handsaker,B., Wysoker,A., Fennell,T., Ruan,J., Homer,N., Marth,G., Abecasis,G. and Durbin,R. (2009) The Sequence Alignment/Map format and SAMtools. *Bioinformatics*, **25**, 2078–2079.
25. Quinlan,A.R. and Hall,I.M. (2010) BEDTools: A flexible suite of utilities for comparing genomic features. *Bioinformatics*, **26**, 841–842.
26. Zhang,Y., Liu,T., Meyer,C.A., Eeckhoute,J., Johnson,D.S., Bernstein,B.E., Nusbaum,C., Myers,R.M., Brown,M., Li,W., *et al.* (2008) Model-based analysis of ChIP-Seq (MACS). *Genome Biol.*, **9**, R137.
27. Vara,C., Paytuvi-Gallart,A., Cuartero,Y., Le Dily,F., Garcia,F., Salva-Castro,J., Gomez,H.L., Julia,E., Moutinho,C., Aiese Cigliano,R., *et al.* (2019) Three-Dimensional Genomic Structure and Cohesin Occupancy Correlate with Transcriptional Activity during Spermatogenesis. *Cell Rep*, **28**, 352-367 e9.
28. Pascual-Reguant,L., Blanco,E., Galan,S., Le Dily,F., Cuartero,Y., Serra-Bardenys,G., Di Carlo,V., Iturbide,A., Cebrià-Costa,J.P., Nonell,L., *et al.* (2018) Lamin B1 mapping reveals the existence of dynamic and functional euchromatin lamin B1 domains. *Nat. Commun.*, **9**, 3420.
29. Serra,F., Baù,D., Goodstadt,M., Castillo,D., Filion,G. and Marti-Renom,M.A. (2017) Automatic analysis and 3D-modelling of Hi-C data using TADbit reveals structural features of the fly chromatin colors. *PLoS Comput. Biol.*, **13**, e1005665.
30. Marco-Sola,S., Sammeth,M., Guigó,R. and Ribeca,P. (2012) The GEM mapper: Fast, accurate and versatile alignment by filtration. *Nat. Methods*, **9**, 1185–1188.
31. Imakaev,M., Fudenberg,G., McCord,R.P., Naumova,N., Goloborodko,A., Lajoie,B.R., Dekker,J. and Mirny,L.A. (2012) Iterative correction of Hi-C data reveals hallmarks of chromosome organization. *Nat. Methods*, **9**.
32. Serra,F., Baù,D., Filion,G. and Marti-Renom,M. (2016) Structural features of the fly chromatin colors revealed by automatic three-dimensional modeling. *bioRxiv*, 10.1101/036764.
33. Heinz,S., Benner,C., Spann,N., Bertolino,E., Lin,Y.C., Laslo,P., Cheng,J.X., Murre,C., Singh,H. and Glass,C.K. (2010) Simple Combinations of Lineage-Determining Transcription Factors Prime cis-Regulatory Elements Required for Macrophage and B Cell Identities. *Mol. Cell*, **38**, 576–589.
34. Russel,D., Lasker,K., Webb,B., Velázquez-Muriel,J., Tjioe,E., Schneidman-Duhovny,D., Peterson,B. and Sali,A. (2012) Putting the pieces together: Integrative modeling platform software for structure determination of macromolecular assemblies. *PLoS Biol.*, **10**, e1001244.
35. Baù,D. and Marti-Renom,M.A. (2012) Genome structure determination via 3C-based data integration by the Integrative Modeling Platform. *Methods*, **58**, 300–6.
36. Corces,M.R., Trevino,A.E., Hamilton,E.G., Greenside,P.G., Sinnott-Armstrong,N.A.,

Vesuna,S., Satpathy,A.T., Rubin,A.J., Montine,K.S., Wu,B., *et al.* (2017) An improved ATAC-seq protocol reduces background and enables interrogation of frozen tissues. *Nat. Methods*, **14**, 959–962.

37. Ernst,J. and Kellis,M. (2012) ChromHMM: automating chromatin-state discovery and characterization. *Nat. Methods*, **9**, 215–216.
38. Ryan,D.P. and Tremethick,D.J. (2018) The interplay between H2A.Z and H3K9 methylation in regulating HP1 binding to linker histone-containing chromatin. *Nucleic Acids Res.*, **46**, 9353–9366.
39. Chandra,T., Ewels,P.A., Schoenfelder,S., Furlan-Magaril,M., Wingett,S.W., Kirschner,K., Thuret,J.Y., Andrews,S., Fraser,P. and Reik,W. (2015) Global reorganization of the nuclear landscape in senescent cells. *Cell Rep.*, **10**, 471–83.
40. Geeven,G., Zhu,Y., Kim,B.J., Bartholdy,B.A., Yang,S.M., Macfarlan,T.S., Gifford,W.D., Pfaff,S.L., Verstegen,M.J., Pinto,H., *et al.* (2015) Local compartment changes and regulatory landscape alterations in histone H1-depleted cells. *Genome Biol*, **16**, 289.
41. Yusufova,N., Kloetgen,A., Teater,M., Osunsade,A., Camarillo,J.M., Chin,C.R., Doane,A.S., Venters,B.J., Portillo-Ledesma,S., Conway,J., *et al.* (2021) Histone H1 loss drives lymphoma by disrupting 3D chromatin architecture. *Nature*, **589**, 299–305.
42. Willcockson,M.A., Healton,S.E., Weiss,C.N., Bartholdy,B.A., Botbol,Y., Mishra,L.N., Sidhwani,D.S., Wilson,T.J., Pinto,H.B., Maron,M.I., *et al.* (2021) H1 histones control the epigenetic landscape by local chromatin compaction. *Nature*, **589**, 293–298.
43. Woodcock,C.L., Skoultchi,A.I. and Fan,Y. (2006) Role of linker histone in chromatin structure and function: H1 stoichiometry and nucleosome repeat length. *Chromosome Res.*, **14**, 17–25.
44. Meshorer,E., Yellajoshula,D., George,E., Scambler,P.J., Brown,D.T. and Misteli,T. (2006) Hyperdynamic plasticity of chromatin proteins in pluripotent embryonic stem cells. *Dev. Cell*, **10**, 105–116.
45. Terme,J.M., Sesé,B., Millán-Ariño,L., Mayor,R., Belmonte Izpisúa,J.C., Barrero,M.J. and Jordan,A. (2011) Histone H1 variants are differentially expressed and incorporated into chromatin during differentiation and reprogramming to pluripotency. *J. Biol. Chem.*, **286**, 35347–35357.
46. Pan,C. and Fan,Y. (2016) Role of H1 linker histones in mammalian development and stem cell differentiation. *Biochim. Biophys. Acta Protein Struct. Mol. Enzymol.*, **1859**, 496–509.
47. Scaffidi,P. (2016) Histone H1 alterations in cancer. *Biochim. Biophys. Acta - Gene Regul. Mech.*, **1859**, 533–539.

FIGURE LEGENDS

Figure 1. Genomic redistribution of histone H1 variants upon H1 knock-down in breast cancer cells. (A) Immunoblot analysis of H1 depletion in multiH1 KD cells. Chromatin extracts (1 or 5µg of protein) from T47D multiH1 KD cells cultured in the presence or not of Doxycycline for 6 days were run in SDS/PAGE and immunoblotted with the indicated antibodies against H1 variants or histone H3 as loading control. **(B)** ChIP-qPCR of H1 variants in multiH1 KD cells. Chromatin from untreated or Dox-treated H1 KD cells was used for ChIP with antibodies against H1 variants and unrelated IgG as a control. Resulting DNA was amplified by qPCR with oligos for distal promoter (3kb upstream TSS) and TSS regions of genes *CDK2* and *NANOG*. ChIP amplification is shown relative to input DNA amplification. A representative experiment quantified in triplicate is shown. **(C)** Box plots showing H1 variants input-subtracted ChIP-seq abundance within G bands, for each band type (Gneg1-4 and Gpos25-100), in multiH1 KD cells treated or not with Doxycycline. GC content of G bands for each band type is also represented. Gneg bands were divided in 4 equal groups according to GC content. Wilcoxon signed-rank test was used to compare the H1 variants abundance within G bands before and after multiH1 KD: (***) $P < 0.001$; (**) $P < 0.01$; (*) $P < 0.05$. Gpos25, N = 87; Gpos50, N = 121; Gpos75, N = 89; Gpos100, N = 81; Gneg, N = 414. Data corresponds to a representative ChIP-seq experiment. **(D)** Scatter plots of the indicated H1 variant pairs input-subtracted ChIP-seq abundance within 100-kb bins of the human genome. The GC content at each bin is color-coded. Pearson's correlation coefficient is shown (*P*-value<0.001). **(E)** Scatter plots of H1 variants input-subtracted ChIP-seq abundance within 100-kb bins of the human genome in multiH1 KD cells treated or not with Doxycycline. The GC content at each bin is color-coded. **(F)** Heat map and cluster analysis of the input-subtracted ChIP-seq abundance of H1 variants and H3K9me3 from WT or H1 KD T47D cells (-/+Dox) within 10 chromatin states (ChromHMM segmentation).

Figure 2. A/B compartments redistribution upon multiH1 KD. (A) Scatter plot of principal component coefficients (PC1) for 100-kb genomic segments (bins) from WT (-Dox) and multiH1 KD (+Dox) cells. PC coefficients were used to define A (positive PC) and B (negative PC) compartments, as well as compartment shifting (A-to-B and B-to-A), compaction (blue bins AA-A and BB+B) and decompaction (red bins AA+A and BB-B) upon H1 KD. Unchanged segments AA and BB are black-colored. A polynomial regression line was used to model the relationship between the dependent and the independent variables. **(B)** A/B compartments redistribution within chromosomes. Scatter plot between the percentage of bins within compartments A or B, or that changed from A to B or vice versa upon H1 KD, and the average H1.2/H1X ChIP-seq signal ratio within TADs, for each chromosome. Spearman's correlation coefficient is shown as well as *P*-value. **(C)** Schematic representation and bins counting for each

category (unchanged, compaction and decompaction) obtained in (**A**). **(D)** Gene expression changes upon H1 KD within bins changing compartment or compaction rate. Normalized RNA-seq reads of coding and non-coding genes before and after Dox-induced H1 KD within 100-kb bins of the 8 categories shown in (**C**) were used to calculate the +/-Dox fold-change (expressed as log2). On the right, the total number of genes found within the bins is shown for each category, as well as the number of up- and down-regulated genes upon H1 KD, considering fold-change ≥1.4. **(E)** Scatter plot of principal component (PC1) in WT (-Dox) cells against the input-subtracted ChIP-seq H1.2 or H1X signal within 100-kb bins. Spearman's correlation coefficient is shown (*P*-value<0.001). Bar plot in the right shows the proportion of the occupancy of chromatin states within a subset of 100-kb bins defined by low A compartment value (0<PC1<30) and low H1.2 signal (<-0.005). The base pair overlap between chromatin states fragments and selected bins was calculated and represented as percentage to the total. Color legend is shown in (**F**). **(F)** Proportion of the occupancy of chromatin states within within 100-kb bins of the 8 categories described in (**C**). **(G-H)** Box plot showing H1 variants input-subtracted ChIP-seq signal within bins of each category in WT cells (-Dox) (**G**), or the ratio of change (log2) in H1 KD (+Dox) compared to untreated cells (-Dox) (**H**). (***) P < 0.001; (**) P < 0.01; (*) P < 0.05. Kruskal-Wallis test determined that there were statistically significant differences between the groups (P < 0.001). One-sample Wilcoxon signed-rank test was used to compare each group of bins against the median gene expression changes (D), H1 variants input-subtracted ChIP-seq signal (G), or ratio of change (H).

Figure 3. TAD border changes upon H1 KD. (A) Box plot showing number of TADs per chromosome in multiH1 KD cells treated (KD) or not (WT) with Doxycycline. Mann-Whitney test did not identify significant differences between the two conditions. **(B)** Box plot showing the conservation of TAD borders in H1 KD compared to WT cells. **(C)** Bar plots showing the frequency of overlap between genome segments (100-kb bins) within A/B compartment categories described in Figure 2C and TAD borders which have been divided in conserved, shifted <100kb and non-conserved according to their behavior upon H1 KD. The observed and expected count of bins of the different groups of TADs were significantly different (P < 0.001, Pearson's Chi-squared test). **(D)** Box plot showing the H1.2 and H1.4 input-subtracted ChIP-seq signal in WT cells within TADs containing the TAD borders divided in conserved, shifted <100kb and non-conserved. **(E)** Bar plot showing differences upon H1 KD in the distribution of TADs border strength (from 1 to 10, being 10 the strongest). H1 KD produces a decrease in the frequency of strong TAD borders. **(F)** TAD border dynamics. Box plot of normalized border strength distribution for TAD borders in WT and H1 KD cells, divided in conserved, shifted <100kb and non-conserved borders. **(G)** Box plots showing TAD border strength per TAD at WT and H1 KD (-/+Dox) cells, distinguishing whether TADs overlap with A or B compartment or both. AB means TADs overlapping partially A and

B compartments simultaneously. (*) P < 0.05 (Mann-Whitney test). (D,F,G) (***) P < 0.001; (**) P < 0.01; (*) P < 0.05 (Mann-Whitney test).

Figure 4. Dynamics of Hi-C genomic interactions and chromatin changes upon H1 KD. (A) Plot comparing the distribution of Hi-C interactions versus genomic distance across the genome for a maximum distance of 500 Mb for WT and H1 KD cells. **(B)** Increased (red colored) and decreased (blue colored) interactions in contact matrices of chromosome 11 (0-135Mb) and chromosome 17 (0-81Mb), of WT and H1 KD cells, at 100kb bins resolution. **(C)** Box plot showing average number of differential intra- or inter-TAD interactions per chromosome upon H1 KD in different compartments, at 100 kb resolution. The average number per chromosome of differential interactions for each category is indicated in the ticks of X axes. **(D-E)** Box plots showing the relative number of ATAC-seq peaks (normalized by length) within A/B compartments (**D**) or within TADs classified according to H1.2/H1X ratio (Groups 1 to 4) (**E**), at WT and H1 KD (-/+Dox) cells. The ChIP-seq H1.2/H1X signal ratio within TADs in the 4 groups reported is shown for reference in (**E**). **(F)** Box plots showing the H3K9me3 input-subtracted ChIP-seq signal within A/B compartments (left) or within TADs classified according to H1.2/H1X ratio (right), at WT and H1 KD (-/+Dox) cells. (D-F) (***) P < 0.001; Wilcoxon signed-rank test. A compartment, N = 1,057; B compartment, N = 1,009; TADs, N = 735 TADs per group.

Figure 5. H1 content of TADs containing genes up- or down-regulated upon multiH1 KD. (A) Volcano plot of gene expression changes upon multiH1 KD measured by RNA-seq. Log2 of fold change is plotted against the minus log10 of *P*-value. Green dots mark genes with a FC≥±1.4 and *P*<0.05. Interferon stimulated genes (ISGs) (*P*-value<1e-100) are labeled (blue dots). **(B)** Box plot showing the gene expression change upon H1 KD (+/-Dox), Log2 of ChIP-seq H1.2/H1X ratio (data from WT cells), normalized gene richness and normalized basal gene expression within TAD groups: all TADs, TADs without deregulated genes upon H1 KD (Control), TADs containing only up-regulated genes, only down-regulated, or both up- and down-regulated genes simultaneously (FC≥±1.4, *P*<0.05). **(C)** Box plot showing H1 variants input-subtracted ChIP-seq signal from WT (-Dox) and H1 KD (+Dox) cells within the TAD groups described in (B). **(D)** Bar plots showing the frequency of overlap between all the TAD groups described in (B) and genome segments within A/B compartment categories described in Figure 2C. There were significant differences between the observed and expected count of bins of the different groups of TADs (P < 0.001, Pearson's Chi-squared test). **(E-G)** Box plot showing ATAC-seq accessibility gain (**E**), changes in H3K9me3 ChIP-seq signal (**F**) and changes in intra-TAD interactions (**G**) upon H1 KD (+/-Dox) within the TAD groups described in (B). (B-C,E-G) (***) P < 0.001; (**) P < 0.01; (*) P < 0.05 (Mann-Whitney test).

Figure 6. Gene expression is coordinately altered within TADs upon H1 KD. (A) (Top panel) Histogram of the frequencies of TADs for the observed (gray) or randomized (purple) position of genes, for TADs containing an increasing proportion of genes per TAD with positive FC. Observed and expected values were compared using Pearson's chi-square test. Gene locations were randomized 10,000 times, constraining by chromosome, not allowing overlapping, and only considering TADs with ≥4 genes. (Bottom panel) Ratio of observed versus expected frequencies of TADs with distinct proportions of genes with positive or negative H1 KD-induced FC; FC>1 or FC<-1. **(B)** TADs with ≥4 genes where at least 90% of genes are down- (left) or up-regulated (right) with FC<-1 or FC>1, respectively (total N=107). Log2 of FC is shown. TADs are ordered from low to high abundance of genes per TAD. Dashed lanes indicate FC=-1.4 or FC=1.4. Red dots represent ISGs. Example genes shown in (**C**) are located within TADs marked with an arrow. **(C)** Examples of TADs with biased coordinated response to H1 KD. Fold change +Dox/-Dox (log2) is shown for all coding and non-coding genes present within a representative TAD containing 90-100% of genes with negative (left) or positive (right) FC, respectively. Genes are ordered according to their position within the genome. Red asterisk represent ISGs. **(D)** Box plot showing the ChIP-seq H1.2/H1X log2 ratio within TADs in the 10 groups described in (**A**). **(E)** Box plot showing the ATAC-seq accessibility gain upon H1 KD (+/-Dox) within TADs in the 10 groups described in (**A**). Kruskal-Wallis test determined that there were statistically significant differences between the groups in (D) and (E). Comparison between each group of TADs and the median ChIP-seq H1.2/H1X log2 ratio (D) or the ATAC-seq accessibility changes (E) was performed using the one-sample Wilcoxon signed-rank test (***) P < 0.001; (**) P < 0.01. **(F)** Bar plot showing the percentage of bp overlapping between A or B compartment and the 10 groups described in (A). **(G)** Bar plots showing the frequency of overlap between all the TAD groups described in (**A**) and genome segments within A/B compartment categories described in Figure 2C that changed compaction upon H1 KD. The observed and expected count of bins of the different groups of TADs were significantly different (P < 0.001, Pearson's Chi-squared test).

Figure 7. Structural properties of TADs. Violin plots of structural properties measured on the 3D models computed for 7 classes of TADs, both in WT and H1 KD conditions (-/+Dox): TADs with the most extreme H1.4 decrease upon H1 KD (*h1*, N=100), TADs presenting a bidirectional transcriptional response to multi-H1 KD (*bi*, N=181), TADs presenting the minimum gene expression changes (*mi*, N=100), TADs presenting a coordinated transcriptional response to H1 KD (*u*, only up-regulated genes, N=71; *d*, only down-regulated genes, N=36; *ud*, TADs *u* and *d* together, N=107), and TADs without genes (*wi*, N=10). For each TAD, 1000 models have been generated and clustered, and plotted measures are relative to the main cluster of models. Obtained measures were consistency, radius of gyration, walking angle (shown in Suppl. Figure

10), and density (shown here). Matrices next to violin plots indicate classes of TADs that are significantly different for each measure. Statistical significance of the difference between distributions was computed with Kolmogorov-Smirnov test (*P*-value<0.01). See *Materials and Methods* for details.

Figure 8. Chromatin organization and consequences upon H1 depletion on genome structure. *Chromatin organization and H1 variants distribution (upper panel):* Hi-C data allows determination of B (inactive) and A (active) compartments. B compartment is characterized by closed chromatin, long TADs with a high H1.2/H1X ratio and a great overlap with low GC Giemsa bands, while the opposite occurs for A compartment (20). H1 variants were differentially distributed along the genome and two profiles could be distinguished in T47D breast cancer cells: H1.2, H1.5 and H1.0 co-localized at low GC regions whereas H1.4 and H1X occupied high GC regions. Upon multiple H1 depletion (H1 KD), H1.2 and H1.4 were strongly depleted while H1.0 became up-regulated but without changing its distribution. Remaining H1.4 redistributed to low GC regions, whereas H1.2, H1.5 and especially H1X were redistributed to higher GC regions. *Consequences of H1 KD in chromatin structure (middle panel):* Upon H1 KD, chromatin accessibility increased and H3K9me3 signal decreased, especially at A compartment. H3K9me3 broad peaks were lost in B compartment. Inter-TAD interactions decreased both at B and A compartments whereas intra-TAD interactions were reduced more importantly at A compartment. TAD-border strength decreased at A compartment, together with some TAD borders being lost or shifted. Upon H1 KD, shifts between and within A/B compartments occurred, being more frequent compaction shifts at A compartment (including A-to-B shifts) and decompaction at B compartment (incl. B-to-A). *Consequences of H1 KD in genome structure are related to gene expression deregulation (bottom panel):* TADs presenting a coordinated response to H1 KD were enriched compared to the expected frequency. Up-regulated genes accumulated within TADs with poor basal expression and low gene density. Gene-dense TADs contained both up- and down-regulated genes simultaneously. TADs with only down-regulated genes showed intermediate features.

Figure 1

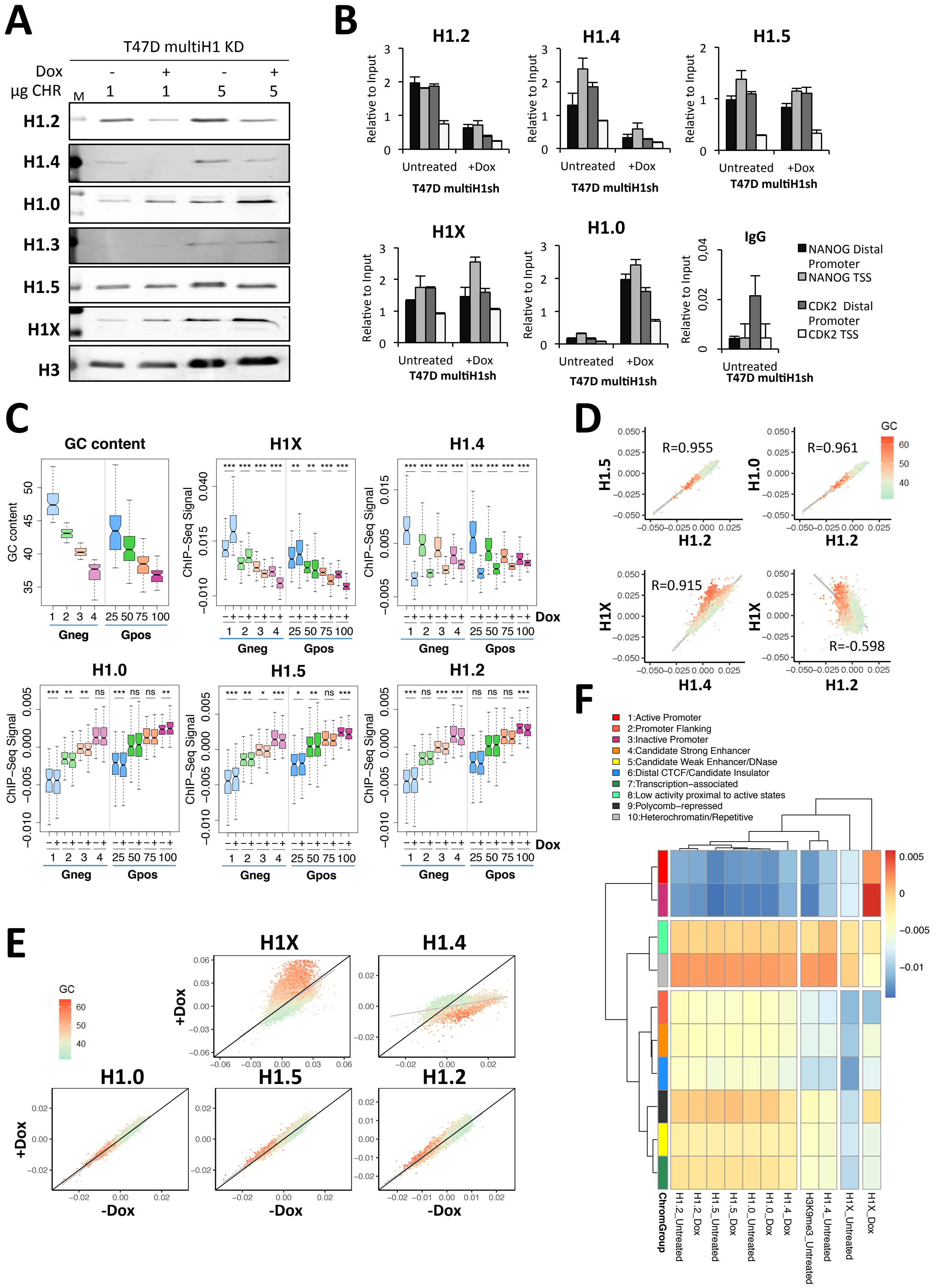
A
T47D multiH1 KD
Dox - + - +
µg CHR 1 1 5 5
M
H1.2
H1.4
H1.0
H1.3
H1.5
H1X
H3
B
H1.2
H1.4
H1.5
H1X
H1.0
IgG
Relative to Input
Untreated +Dox
T47D multiH1sh
■ NANOG Distal Promoter
■ NANOG TSS
■ CDK2 Distal Promoter
□ CDK2 TSS
C
GC content
H1X
H1.4
H1.0
H1.5
H1.2
ChIP−Seq Signal
1 2 3 4 25 50 75 100
Gneg Gpos
Dox
D
R=0.955
R=0.961
R=0.915
R=-0.598
H1.5
H1.0
H1X
H1.2
H1.4
GC
60
50
40
E
H1X
H1.4
H1.0
H1.5
H1.2
+Dox
-Dox
GC
F
1:Active Promoter
2:Promoter Flanking
3:Inactive Promoter
4:Candidate Strong Enhancer
5:Candidate Weak Enhancer/DNase
6:Distal CTCF/Candidate Insulator
7:Transcription−associated
8:Low activity proximal to active states
9:Polycomb−repressed
10:Heterochromatin/Repetitive
0.005
0
−0.005
−0.01
ChromGroup
H1.2_Untreated
H1.2_Dox
H1.5_Untreated
H1.5_Dox
H1.0_Untreated
H1.0_Dox
H1.4_Dox
H3K9me3_Untreated
H1.4_Untreated
H1X_Untreated
H1X_Dox

Figure 2

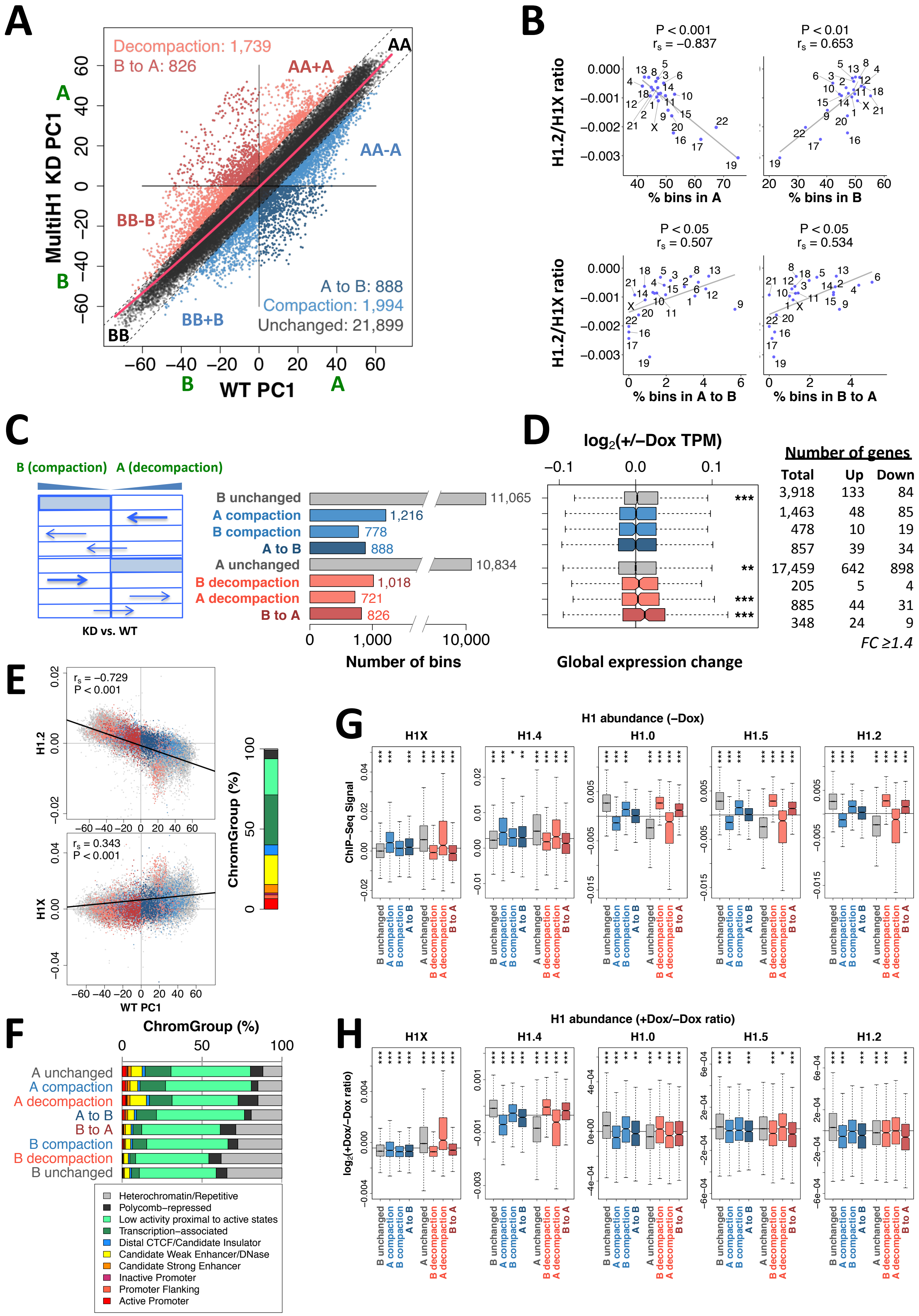
A
Decompaction: 1,739
B to A: 826
AA+A
AA
AA-A
BB-B
A to B: 888
Compaction: 1,994
Unchanged: 21,899
BB+B
BB
MultiH1 KD PC1
WT PC1
A
B
B
P < 0.001
r_s = −0.837
P < 0.01
r_s = 0.653
P < 0.05
r_s = 0.507
P < 0.05
r_s = 0.534
H1.2/H1X ratio
% bins in A
% bins in B
% bins in A to B
% bins in B to A
C
B (compaction)
A (decompaction)
KD vs. WT
B unchanged 11,065
A compaction 1,216
B compaction 778
A to B 888
A unchanged 10,834
B decompaction 1,018
A decompaction 721
B to A 826
Number of bins
D
log2(+/−Dox TPM)
Global expression change
Number of genes
Total Up Down
3,918 133 84
1,463 48 85
478 10 19
857 39 34
17,459 642 898
205 5 4
885 44 31
348 24 9
FC ≥1.4
E
r_s = −0.729
P < 0.001
H1.2
r_s = 0.343
P < 0.001
H1X
WT PC1
ChromGroup (%)
F
ChromGroup (%)
A unchanged
A compaction
A decompaction
A to B
B to A
B compaction
B decompaction
B unchanged
Heterochromatin/Repetitive
Polycomb−repressed
Low activity proximal to active states
Transcription−associated
Distal CTCF/Candidate Insulator
Candidate Weak Enhancer/DNase
Candidate Strong Enhancer
Inactive Promoter
Promoter Flanking
Active Promoter
G
H1 abundance (−Dox)
H1X
H1.4
H1.0
H1.5
H1.2
ChIP−Seq Signal
H
H1 abundance (+Dox/−Dox ratio)
H1X
H1.4
H1.0
H1.5
H1.2
log2(+Dox/−Dox ratio)
B unchanged
A compaction
B compaction
A to B
A unchanged
B decompaction
A decompaction
B to A

Figure 3

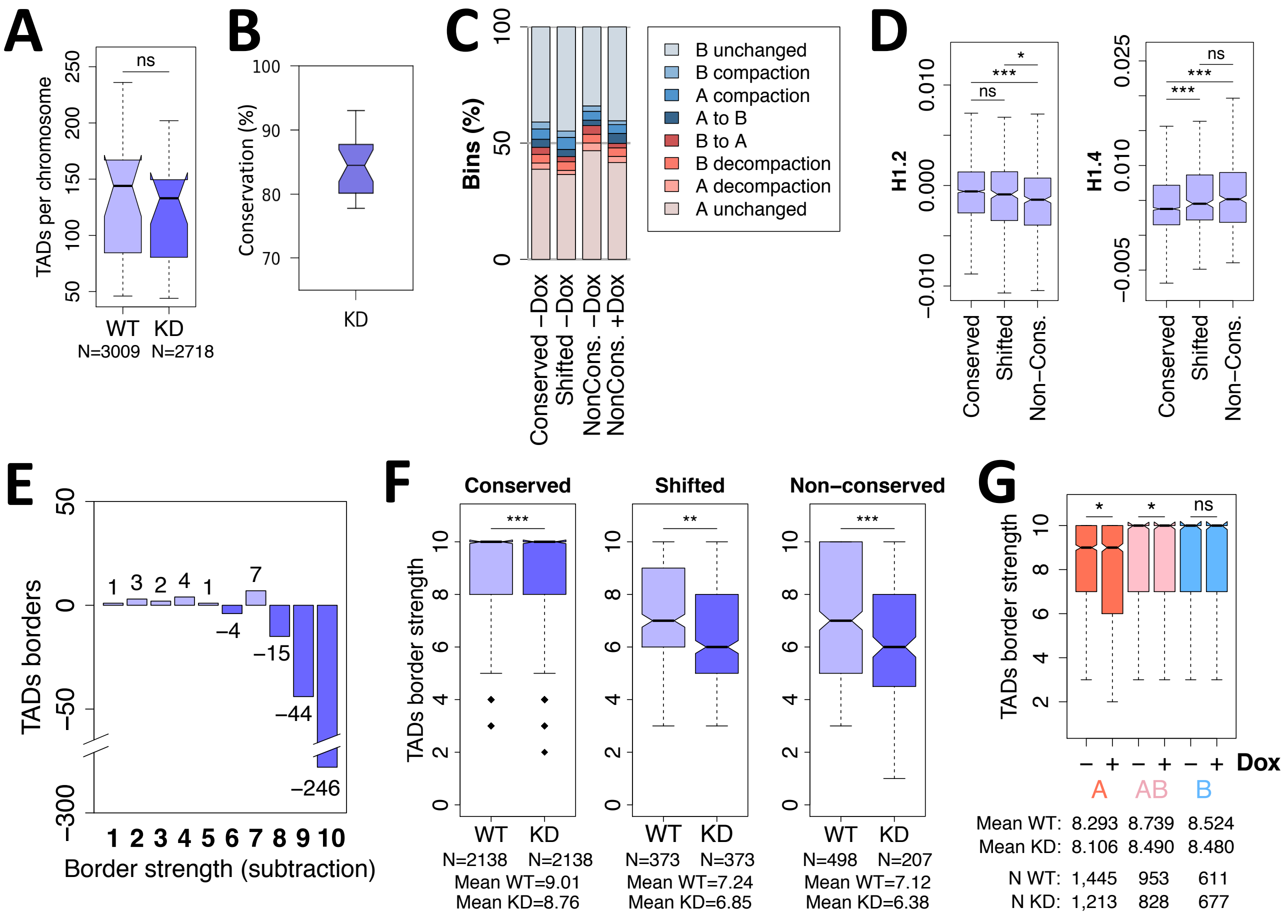
A
TADs per chromosome
50
100
150
200
250
ns
WT
KD
N=3009
N=2718
B
Conservation (%)
70
80
90
100
KD
C
Bins (%)
0
50
100
Conserved −Dox
Shifted −Dox
NonCons. −Dox
NonCons. +Dox
B unchanged
B compaction
A compaction
A to B
B to A
B decompaction
A decompaction
A unchanged
D
H1.2
−0.010
0.000
0.010
ns
***
*
Conserved
Shifted
Non−Cons.
H1.4
−0.005
0.010
0.025
***
***
ns
Conserved
Shifted
Non−Cons.
E
TADs borders
50
0
−50
−300
1
3
2
4
1
−4
7
−15
−44
−246
1 2 3 4 5 6 7 8 9 10
Border strength (subtraction)
F
Conserved
Shifted
Non−conserved
TADs border strength
0
2
4
6
8
10
***
**
***
WT
KD
N=2138
N=2138
Mean WT=9.01
Mean KD=8.76
WT
KD
N=373
N=373
Mean WT=7.24
Mean KD=6.85
WT
KD
N=498
N=207
Mean WT=7.12
Mean KD=6.38
G
TADs border strength
2
4
6
8
10
*
*
ns
− + − + − + Dox
A
AB
B
Mean WT: 8.293 8.739 8.524
Mean KD: 8.106 8.490 8.480
N WT: 1,445 953 611
N KD: 1,213 828 677

Figure 4

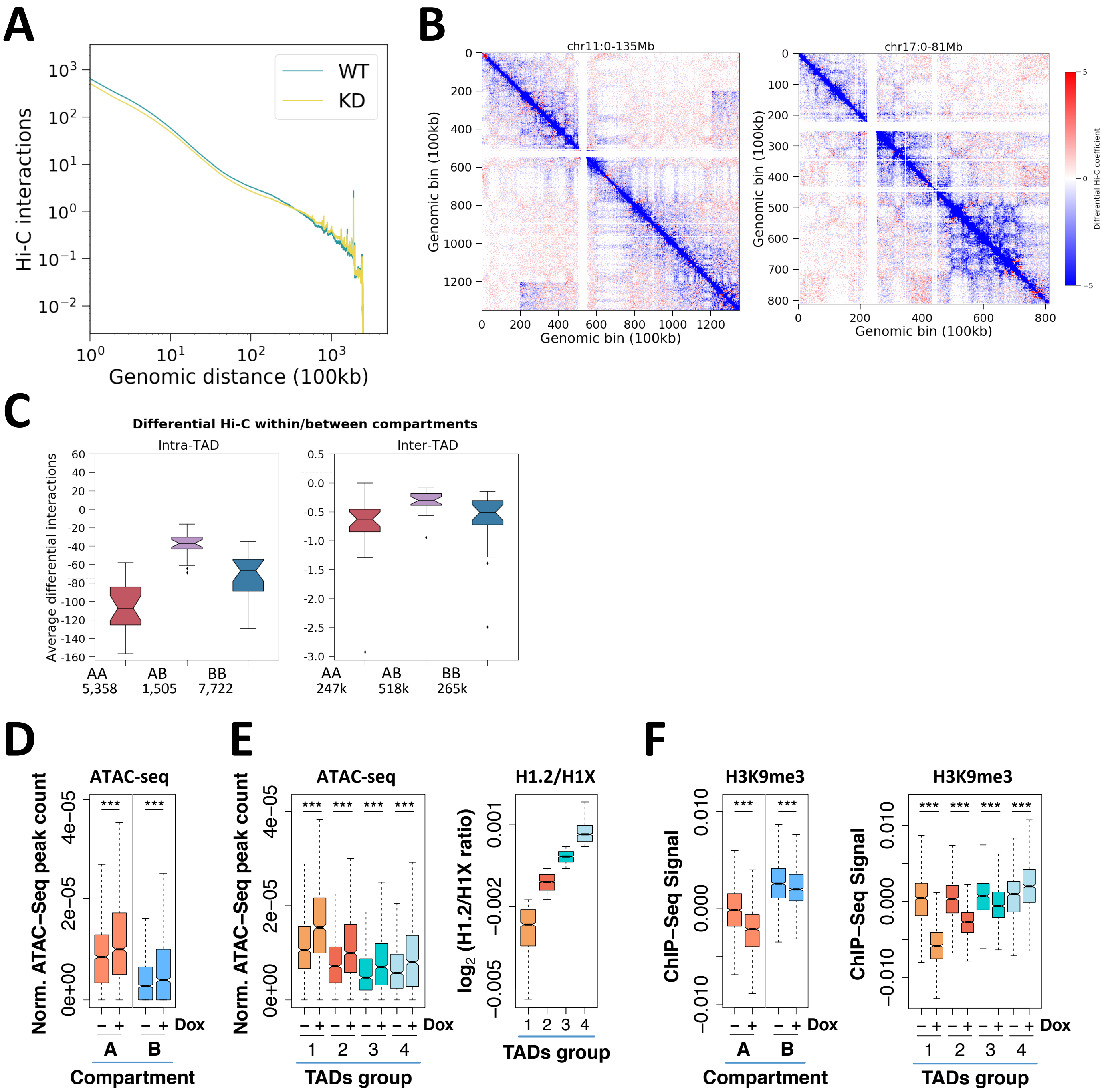
A
Hi-C interactions
Genomic distance (100kb)
WT
KD
10^3
10^2
10^1
10^0
10^{-1}
10^{-2}
10^0
10^1
10^2
10^3
B
chr11:0-135Mb
chr17:0-81Mb
Genomic bin (100kb)
Genomic bin (100kb)
Differential Hi-C coefficient
5
0
−5
C
Differential Hi-C within/between compartments
Intra-TAD
Inter-TAD
Average differential interactions
AA
5,358
AB
1,505
BB
7,722
AA
247k
AB
518k
BB
265k
D
ATAC-seq
Norm. ATAC−Seq peak count
***
***
− + Dox
A
B
Compartment
E
ATAC-seq
Norm. ATAC−Seq peak count
***
***
***
***
− + − + − + − + Dox
1
2
3
4
TADs group
H1.2/H1X
log2 (H1.2/H1X ratio)
1 2 3 4
TADs group
F
H3K9me3
ChIP−Seq Signal
− + − + Dox
A
B
Compartment
H3K9me3
ChIP−Seq Signal
− + − + − + − + Dox
1
2
3
4
TADs group

Figure 5

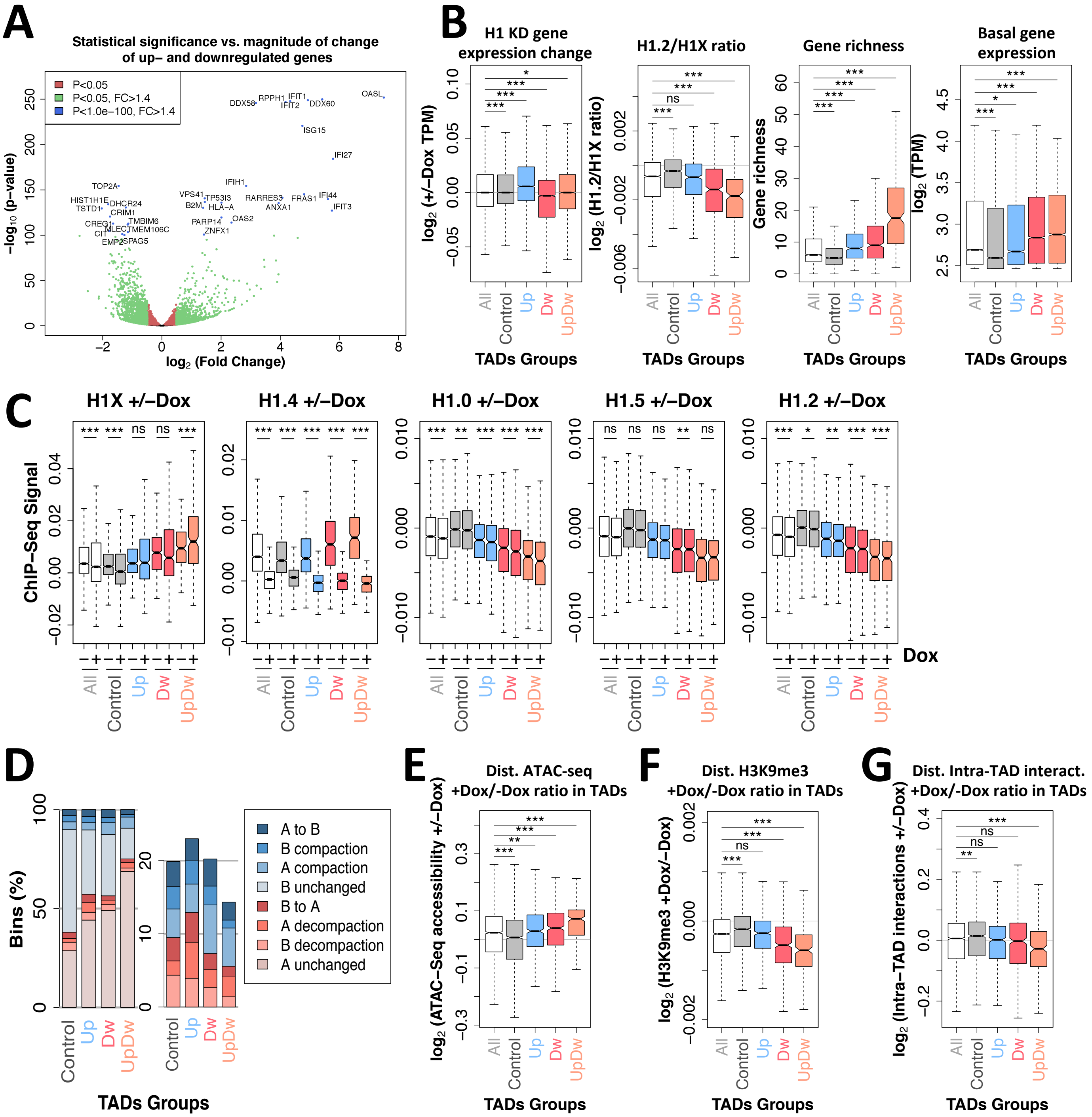
A
Statistical significance vs. magnitude of change of up– and downregulated genes
P<0.05
P<0.05, FC>1.4
P<1.0e−100, FC>1.4
OASL
DDX58
RPPH1
IFIT1
IFIT2
DDX60
ISG15
IFI27
IFIH1
TOP2A
HIST1H1E
DHCR24
TSTD1
CRIM1
CREG1
TMBIM6
MLEC
TMEM106C
CIT
EMP2
SPAG5
VPS41
TP53I3
B2M
HLA−A
RARRES3
ANXA1
FRAS1
IFI44
IFIT3
PARP14
OAS2
ZNFX1
−log10 (p−value)
log2 (Fold Change)
B
H1 KD gene expression change
log2 (+/−Dox TPM)
H1.2/H1X ratio
log2 (H1.2/H1X ratio)
Gene richness
Basal gene expression
log2 (TPM)
All
Control
Up
Dw
UpDw
TADs Groups
*
***
ns
C
H1X +/−Dox
H1.4 +/−Dox
H1.0 +/−Dox
H1.5 +/−Dox
H1.2 +/−Dox
ChIP−Seq Signal
Dox
D
Bins (%)
A to B
B compaction
A compaction
B unchanged
B to A
A decompaction
B decompaction
A unchanged
TADs Groups
E
Dist. ATAC-seq +Dox/-Dox ratio in TADs
log2 (ATAC−Seq accessibility +/−Dox)
F
Dist. H3K9me3 +Dox/-Dox ratio in TADs
log2 (H3K9me3 +Dox/−Dox)
G
Dist. Intra-TAD interact. +Dox/-Dox ratio in TADs
log2 (Intra−TAD interactions +/−Dox)
TADs Groups

Figure 6

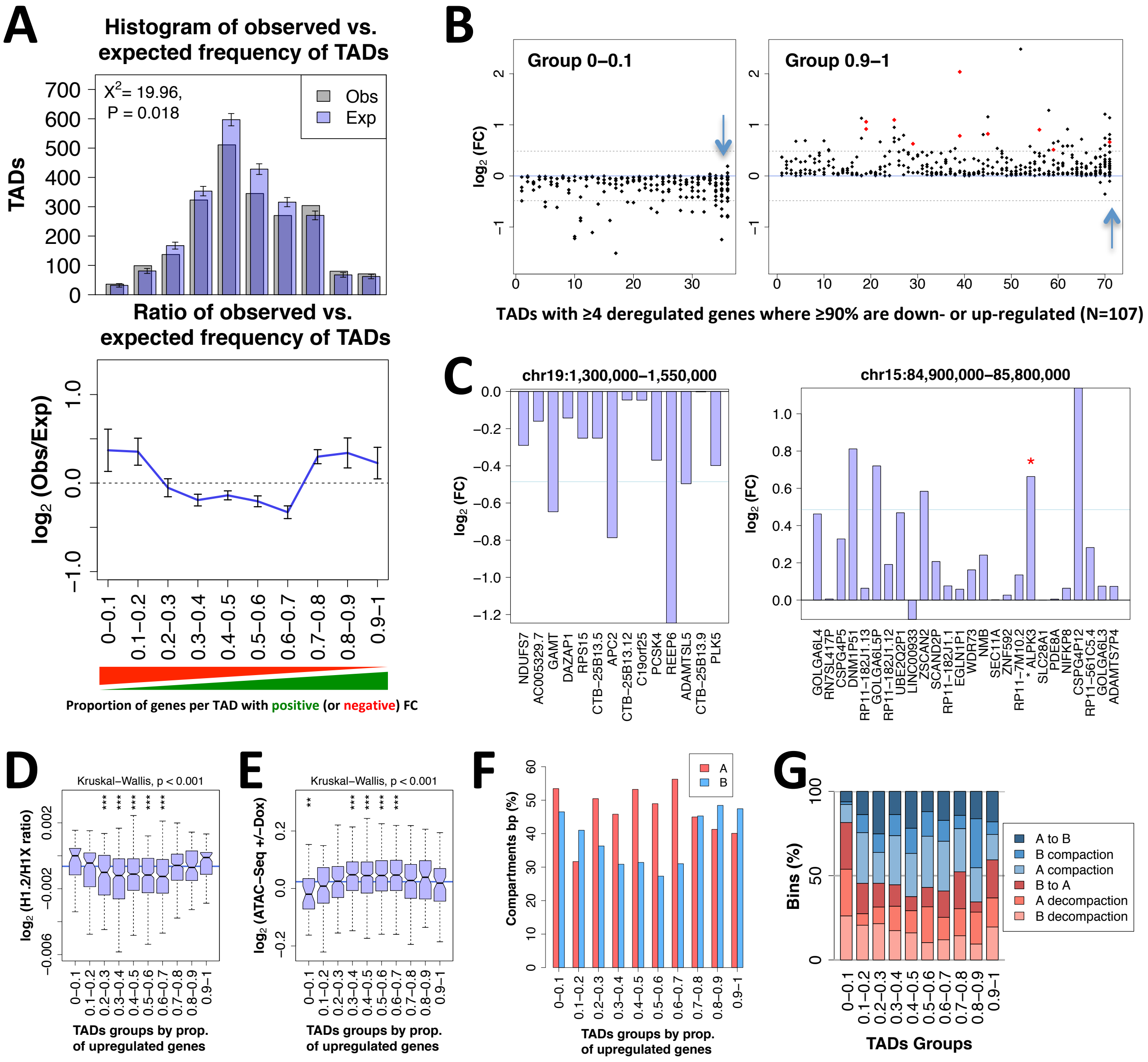
A
Histogram of observed vs. expected frequency of TADs
X^2= 19.96, P = 0.018
Obs
Exp
TADs
0
100
200
300
400
500
600
700
Ratio of observed vs. expected frequency of TADs
$\log_2$ (Obs/Exp)
−1.0
0.0
1.0
0−0.1
0.1−0.2
0.2−0.3
0.3−0.4
0.4−0.5
0.5−0.6
0.6−0.7
0.7−0.8
0.8−0.9
0.9−1
Proportion of genes per TAD with positive (or negative) FC
B
Group 0–0.1
Group 0.9–1
$\log_2$ (FC)
−1
0
1
2
0
10
20
30
40
50
60
70
TADs with ≥4 deregulated genes where ≥90% are down- or up-regulated (N=107)
C
chr19:1,300,000–1,550,000
$\log_2$ (FC)
0.0
−0.2
−0.4
−0.6
−0.8
−1.0
−1.2
NDUFS7
AC005329.7
GAMT
DAZAP1
RPS15
CTB−25B13.5
APC2
CTB−25B13.12
C19orf25
PCSK4
REEP6
ADAMTSL5
CTB−25B13.9
PLK5
chr15:84,900,000–85,800,000
$\log_2$ (FC)
0.0
0.2
0.4
0.6
0.8
1.0
*
GOLGA6L4
RN7SL417P
CSPG4P5
DNM1P51
RP11−182J1.13
GOLGA6L5P
RP11−182J1.12
UBE2Q2P1
LINC00933
ZSCAN2
SCAND2P
RP11−182J1.1
EGLN1P1
WDR73
NMB
SEC11A
ZNF592
RP11−7M10.2
* ALPK3
SLC28A1
PDE8A
NIFKP8
CSPG4P12
RP11−561C5.4
GOLGA6L3
ADAMTS7P4
D
Kruskal–Wallis, p < 0.001
*** *** *** *** ***
$\log_2$ (H1.2/H1X ratio)
−0.006
−0.002
0.002
0−0.1
0.1−0.2
0.2−0.3
0.3−0.4
0.4−0.5
0.5−0.6
0.6−0.7
0.7−0.8
0.8−0.9
0.9−1
TADs groups by prop. of upregulated genes
E
Kruskal–Wallis, p < 0.001
** *** *** *** ***
$\log_2$ (ATAC−Seq +/−Dox)
−0.2
0.0
0.2
0−0.1
0.1−0.2
0.2−0.3
0.3−0.4
0.4−0.5
0.5−0.6
0.6−0.7
0.7−0.8
0.8−0.9
0.9−1
TADs groups by prop. of upregulated genes
F
A
B
Compartments bp (%)
0
10
20
30
40
50
60
0−0.1
0.1−0.2
0.2−0.3
0.3−0.4
0.4−0.5
0.5−0.6
0.6−0.7
0.7−0.8
0.8−0.9
0.9−1
TADs groups by prop. of upregulated genes
G
Bins (%)
0
50
100
A to B
B compaction
A compaction
B to A
A decompaction
B decompaction
0−0.1
0.1−0.2
0.2−0.3
0.3−0.4
0.4−0.5
0.5−0.6
0.6−0.7
0.7−0.8
0.8−0.9
0.9−1
TADs Groups

Figure 7

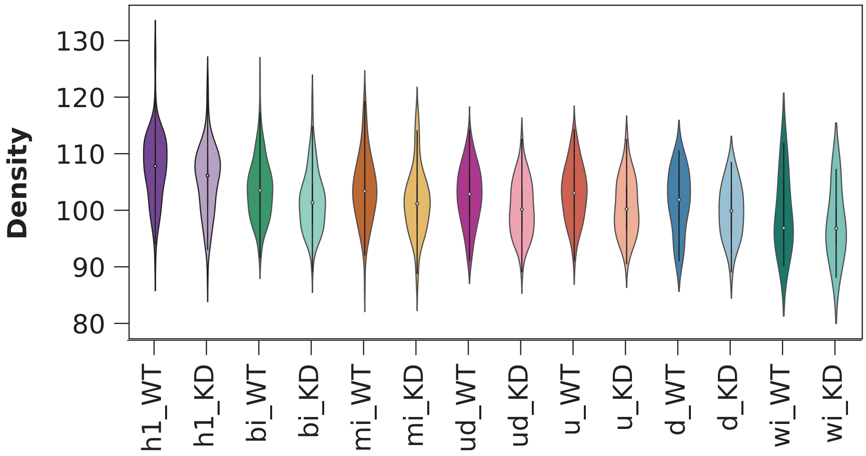

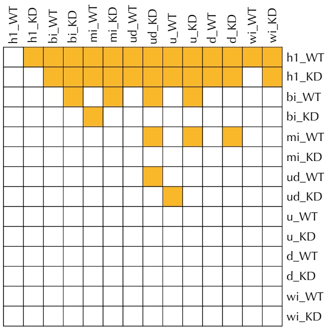

h1_WT	h1_KD	bi_WT	bi_KD	mi_WT	mi_KD	ud_WT	ud_KD	u_WT	u_KD	d_WT	d_KD	wi_WT	wi_KD	
	🟧	🟧	🟧	🟧	🟧	🟧	🟧	🟧	🟧	🟧	🟧	🟧	🟧	h1_WT
		🟧	🟧	🟧	🟧	🟧	🟧	🟧	🟧	🟧	🟧		🟧	h1_KD
			🟧		🟧		🟧		🟧					bi_WT
				🟧										bi_KD
							🟧		🟧		🟧			mi_WT
														mi_KD
							🟧							ud_WT
								🟧						ud_KD
														u_WT
														u_KD
														d_WT
														d_KD
														wi_WT
														wi_KD

Figure 8

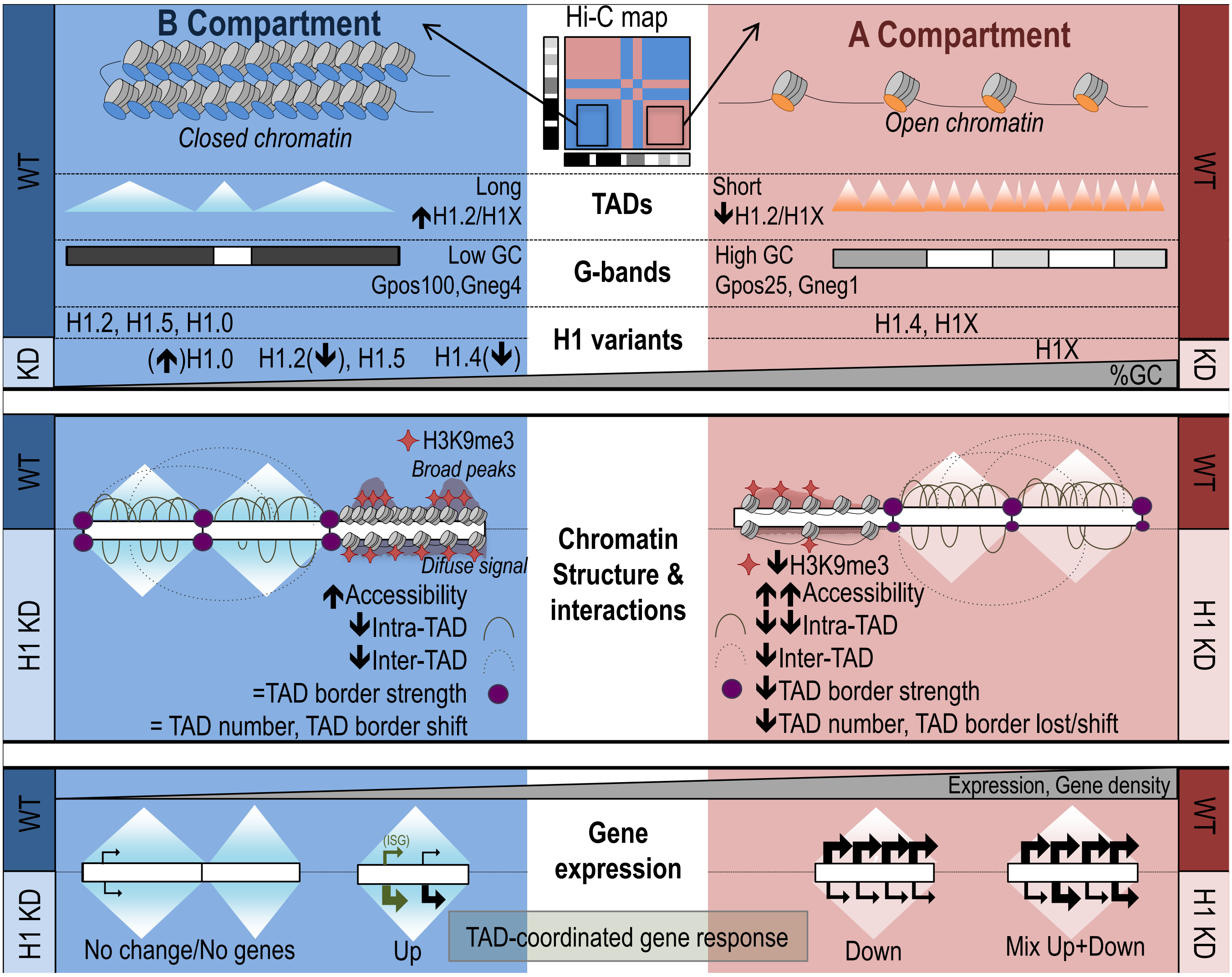
B Compartment
Hi-C map
A Compartment
Closed chromatin
Open chromatin
WT
KD
WT
KD
Long
↑H1.2/H1X
TADs
Short
↓H1.2/H1X
Low GC
Gpos100,Gneg4
G-bands
High GC
Gpos25, Gneg1
H1.2, H1.5, H1.0
H1 variants
H1.4, H1X
(↑)H1.0 H1.2(↓), H1.5 H1.4(↓)
H1X
%GC
WT
H1 KD
WT
H1 KD
H3K9me3
Broad peaks
Difuse signal
↑Accessibility
↓Intra-TAD
↓Inter-TAD
=TAD border strength
= TAD number, TAD border shift
Chromatin Structure & interactions
↓H3K9me3
↑↑Accessibility
↓↓Intra-TAD
↓Inter-TAD
↓TAD border strength
↓TAD number, TAD border lost/shift
WT
H1 KD
WT
H1 KD
Expression, Gene density
Gene expression
(ISG)
No change/No genes
Up
TAD-coordinated gene response
Down
Mix Up+Down